Joint Centre for Mesoscale Meteorology, Reading, UK

The Semigeostrophic Diagnosis of Vertical Motion

Part I: Formulation and co-ordinate transformations

M. A. Pedder
A. J. Thorpe

Internal Report No. 94

September 1998

Met Office Joint Centre for Mesoscale Meteorology Department of Meteorology
University of Reading PO Box 243 Reading RG6 6BB United Kingdom
Tel: +44 (0)118 931 8425 Fax: +44 (0)118 931 8791
www.metoffice.com

Designed and produced by the Met Office © Crown copyright 2001 01/0240 The Met Office logo is a registered trademark.

The Semigeostrophic Diagnosis of Vertical Motion. Part I: Formulation and Co-ordinate transformations

Mike A. Pedder* and Alan J. Thorpe

Department of Meteorology, University of Reading

Revised: 21 September 1998

Abstract:

Theoretical considerations suggest that the semigeostrophic (SG) omega equation should provide a more accurate diagnosis of vertical velocity than the classical quasigeostrophic (QG) omega equation in the presence of significant horizontal variations in static stability and potential vorticity. Only very few previous studies have compared the performance of the two methods applied to either real or simulated data. Furthermore, it is almost certain that such comparisons have been affected by uncertainties associated with transformations between physical and geostrophic momentum (GM) co-ordinates, these being necessary in order to solve the SG omega equation in a form which retains the conceptual simplicity of the QG omega equation. Here we describe an accurate method of mapping between physical and GM co-ordinates which is suitable for operating on a large, discrete data base. The result of an inverse mapping is used to measure the accuracy of the method. This is shown to be sensitive to the chosen grid-point resolution in GM space, which may need to be considerably greater than the given resolution in physical space in order to resolve dynamically significant features in regions of negative geostrophic shear.

* Corresponding author: Department of Meteorology, University of Reading, Earley Gate, PO Box 243, Reading RG6 6BB, UK.

The SG equations do not apply when the Jacobian of the GM co-ordinate transformation (J) changes sign within the domain of the analysis. If such a situation occurs with real data, then it is necessary to apply an adjustment to the sampled geopotential (or pressure) data in order to satisfy the condition $J>0$ everywhere prior to a SG diagnosis of vertical velocity. A variational approach to this problem is described and tested using data generated by a primitive equation model of a developing cyclone.

1. Introduction

For extra-tropical weather systems the quasigeostrophic (QG) model is often used to interpret the synoptic scale aspects of their structure and evolution (see, for example, Holton, 1972; Carlson 1991; Rotunno et al., 1994). QG theory has at its core the conservation of QG potential vorticity and a diagnostic equation for the vertical motion, the so called omega equation. The omega equation shows explicitly that the ageostrophic motion is, in dynamical terms, a consequence of the geostrophic motion. Given the importance of vertical motion in generating weather elements such as cloud and precipitation, the omega equation has a special significance for synoptic interpretation and forecasting.

The conservation of QG potential vorticity requires that the state of the atmosphere be divided into a basic state and a deviation from that state. Under QG theory, horizontal variations in the basic state stratification are ignored. This is clearly a very poor approximation when applying the QG model to atmospheric data where typically a large horizontal gradient of stratification occurs at the tropopause. This limitation of the QG system is serious where the horizontal scale of the stratification gradient is on the mesoscale, when the scalings assumed in the QG theory break down. QG theory also ignores the contribution from ageostrophic motion in the horizontal advection of vorticity and temperature, which is unrealistic in regions of strong trajectory curvature.

It has been proposed that the above failings of the QG theory can be alleviated by use of the semigeostrophic (SG) formulation of the equations of motion (Hoskins, 1975). Under SG theory a more accurate estimation of a particle trajectory is used for

advection by incorporating the ageostrophic part of the horizontal wind. This allows for a more accurate representation of the development of mesoscale features, such as those that occur at fronts. Hoskins and Draghici (1977) showed that SG theory leads to a form of omega equation (the SG omega equation) which is very similar in form to the QG omega equation, but in which spatial location variables are replaced by geostrophic momentum (GM) co-ordinate variables. They were thus able to demonstrate that a SG diagnosis of vertical velocity could be obtained by integrating the SG omega equation in GM space, followed by a transformation of the solution from GM to physical co-ordinates

Although there have been many diagnostic studies based on solving various forms of the QG omega equation (see Räisänen (1995) for a useful review), very few have attempted to compare QG and SG solutions. An early study by Bosart and Lin (1984) reported the result of a comparison as part of a diagnostic analysis of an East-Coast storm over North America. They concluded that the SG solution gave vertical velocities closer to those inferred from an operational primitive equation (PE) model analysis, but did not present details of either methodology or the relative accuracy of the various estimates. Graham (1991) compared QG and SG solutions derived from an operational analysis of a cyclone over the N. Atlantic. He concluded that the SG diagnosis of vertical velocity was closer to the PE solution in some regions, though he also noted the difficulty in interpreting results given that the PE model analysis probably reflected in part the influence of diabatic and surface processes which were not represented in the SG analysis. In a more recent study, Pinot et al. (1996) compared solutions given by both SG and various forms of the QG omega equation applied to data generated by an idealised PE model simulation of a baroclinic development in the ocean. They found that their SG solution was less biased than a

'classical' QG solution, especially in regions of descent, but nevertheless differed substantially from the PE model solution in regions of significant ageostrophic circulation.

Both Graham (1991) and Pinot et al. (1996) noted certain technical difficulties in obtaining realistic SG solutions, which do not arise in the case of a QG analysis. These difficulties arise mainly from the need to transform fields sampled in physical (model) space to and from GM co-ordinate space. In the case of Pinot et al.'s study, an approximate method of interpolation was used to generate the data on a regular GM grid prior to solving for the SG vertical velocity by discrete integration of the SG omega equation, followed by an approximate inverse interpolation onto a regular grid in the model space. Graham (1991) applied smoothing operators to data prior to the forward interpolation in order to avoid difficulties associated with either a lack of uniqueness of a transformation or large interpolation errors in regions of negative geostrophic shear. Unfortunately, such manipulations inevitably mean that in practice the vertical velocity given by the SG solution is not necessarily consistent with that implied by the distribution of geostrophic parameters in the model space. None of the aforementioned authors appear to have considered this difficulty, which clearly has implications for the interpretation of differences between the ageostrophic circulations diagnosed by different methods. Here we argue that the problem of accurate transformation between model and GM co-ordinate spaces is crucial for a critical evaluation of SG versus QG diagnosed vertical velocities.

This is Part I of a two-part paper in which we consider the advantages to be gained by using a SG estimation of vertical motion in extra-tropical cyclones. In particular, we examine the accuracy of the recovery of the vertical motion field as well as the role of the undulating tropopause. Since our understanding of extratropical

weather systems is encapsulated in balanced theories, it is essential that a proper and 'fair' test of these theories is carried out on data describing 'real' weather systems. Here in Part I we describe the methodology being employed to obtain the SG vertical velocity whilst in Part 2 we show results of the application of the method to a realistically simulated baroclinic wave life-cycle.

In the following, Section 2 presents a theoretical summary and identifies factors that might limit the accuracy of the SG diagnosis in practice. Section 3 describes actual transformation methods and their limitations, subject to the assumption that the model data can be used to define a unique (one-to-one) mapping between fields sampled in model and GM co-ordinates. Section 4 considers the possibility of applying a SG analysis when the latter condition is not satisfied. Conclusions are presented in section 5.

2. Theoretical Summary

The quasigeostrophic (QG) omega equation arises by using thermal wind balance to remove the time derivatives between the QG vorticity and thermodynamic equations (see, for example, Bluestein, 1992). Here we assume an *f*-plane approximation so that in Cartesian co-ordinates the resulting diagnostic equation for the vertical velocity (w) can be written

$$\overline{N^2}\nabla_h^2 w + f^2 \frac{\partial^2 w}{\partial z^2} = F = 2\nabla_h \cdot \mathbf{Q} \qquad (1)$$

where $\nabla_h = \left(\frac{\partial}{\partial x}, \frac{\partial}{\partial y}\right)$, $\overline{N^2}$ $\left(= \overline{N^2}(z)\right)$ is a horizontally-averaged value of the static stability and f is the Coriolis parameter. The right-hand-side measures the total QG forcing for w, expressed here as twice the divergence of a QG **Q**-vector which is

related to the horizontal derivatives of the geostrophic wind $\mathbf{V}_g \left(=u_g, v_g\right)$ and potential temperature (θ) by

$$\mathbf{Q}=\left(-\frac{g}{\theta_o}\left(\frac{\partial u_g}{\partial x}\frac{\partial \theta}{\partial x}+\frac{\partial v_g}{\partial x}\frac{\partial \theta}{\partial y}\right),-\frac{g}{\theta_o}\left(\frac{\partial u_g}{\partial y}\frac{\partial \theta}{\partial x}+\frac{\partial v_g}{\partial y}\frac{\partial \theta}{\partial y}\right)\right) \tag{2}$$

where θ_o is a constant reference value of the potential temperature. Under the *f*-plane approximation, the geostrophic wind can be related to a geostrophic streamfunction $\psi_g=(p/f\rho)$, where p is pressure and ρ is density, so that

$$\mathbf{V}_g=\left(u_g, v_g\right)=\left(-\frac{\partial \psi_g}{\partial y}, \frac{\partial \psi_g}{\partial x}\right) \tag{3}$$

For the horizontal scales of motion considered under QG theory the hydrostatic approximation applies and $\mathbf{Q}$ can thus be calculated directly from gridded pressure and temperature data.

If we assume a 3-d gridded data-set, such as might arise from an operational analysis or from an idealised numerical model, then it is a straightforward matter to solve (1) using a standard technique such as successive over-relaxation, given appropriate boundary conditions on *w*. Of course $\overline{N^2}(z)$ must also be specified; a representative value may be obtained by averaging over the data domain on a level-by-level basis. A unique solution of (1) is guaranteed only for $\overline{N^2}(z)>0$ everywhere on z (the 'ellipticity' condition). In practice, negative values are unlikely to arise if the averaging is over a sufficiently large horizontal domain, even when there may exist *local* regions of absolute instability within the domain of integration.

The semigeostrophic (SG) omega equation (Hoskins and Draghici, 1977; henceforth HD) plays the same role under SG theory as the QG omega equation plays under QG theory. In the so-called geostrophic-momentum (GM) co-ordinate system,

HD showed that the SG omega equation could be written in a mathematically simple form which is closely analogous to that of the QG omega equation. The co-ordinate variables in GM space are related to those in physical space by

$$X = x + \frac{v_g}{f} \qquad Y = y - \frac{u_g}{f} \qquad Z = z \tag{4}$$

It can then be shown that derivatives in GM space are related to those in physical space by

$$\begin{aligned} \frac{\partial}{\partial X} &= \frac{(1+c)}{J}\frac{\partial}{\partial x} - \frac{b}{J}\frac{\partial}{\partial y} \quad \frac{\partial}{\partial Y} = -\frac{b}{J}\frac{\partial}{\partial x} + \frac{(1+a)}{J}\frac{\partial}{\partial y} \\ \frac{\partial}{\partial Z} &= -\frac{(\alpha(1+c)-\beta b)}{J}\frac{\partial}{\partial x} - \frac{(\beta(1+a)-\alpha b)}{J}\frac{\partial}{\partial y} + \frac{\partial}{\partial z} \end{aligned} \tag{5}$$

in which

$$a = \frac{1}{f}\frac{\partial v_g}{\partial x} \quad c = -\frac{1}{f}\frac{\partial u_g}{\partial y} \quad b = \frac{1}{f}\frac{\partial v_g}{\partial y} = -\frac{1}{f}\frac{\partial u_g}{\partial x} \quad \alpha = \frac{1}{f}\frac{\partial v_g}{\partial z} \quad \beta = -\frac{1}{f}\frac{\partial u_g}{\partial z}$$

In (5) $J = (1 + a + c + ac - b^2)$ is the Jacobian of the co-ordinate transform (4). This is related to a semigeostrophic vorticity ζ_g^* by

$$\zeta_g^* = fJ = \zeta_g + f(ac - b^2) \tag{6}$$

where ζ_g is the geostrophic absolute vorticity. Following HD, the SG omega equation can then be written

$$\frac{g}{f\theta_0}\nabla_H^2 Pw^* + f^2\frac{\partial^2 w^*}{\partial Z^2} = F^* = 2\nabla_H \cdot \mathbf{Q}^* \tag{7}$$

where $\underline{\nabla}_H = \left(\frac{\partial}{\partial X}, \frac{\partial}{\partial Y}\right)$, $w^* = (w / J)$ and $P = \zeta_g^*\frac{\partial\theta}{\partial Z}$ is the SG potential vorticity. In (7), the SG Q-vector is defined by

$$\mathbf{Q}^* = \left(-\frac{g}{\theta_o}\left(\frac{\partial u_g}{\partial X}\frac{\partial \theta}{\partial X} + \frac{\partial v_g}{\partial X}\frac{\partial \theta}{\partial Y} \right), -\frac{g}{\theta_o}\left(\frac{\partial u_g}{\partial Y}\frac{\partial \theta}{\partial X} + \frac{\partial v_g}{\partial Y}\frac{\partial \theta}{\partial Y} \right) \right) \tag{8}$$

It is possible to show that $\mathbf{Q}^*$ and $\mathbf{Q}$ are rather simply related by $\mathbf{Q}^* = \mathbf{Q} / J$ (an identity which appears to have been overlooked in previous work). Hence both w^* and $\mathbf{Q}^*$ differ from their QG counterparts only by a simple scaling which is locally dependent on the magnitude of ζ_g^*. Equation (7) retains the conceptual simplicity of the QG omega equation whilst apparently allowing for a more accurate prediction of w in the presence of significant horizontal variations in P.

Under the f-plane approximation, the geostrophic wind in GM co-ordinate space can be related to a geostrophic streamfunction $\psi_g^* = \psi_g + \frac{1}{2f}\left(u_g^2 + v_g^2\right)$, so that

$$\mathbf{V}_g = \left(u_g, v_g\right) = \left(-\frac{\partial \psi_g^*}{\partial Y}, \frac{\partial \psi_g^*}{\partial X} \right) \tag{9}$$

Hence the SG forcing F^* in (7) can be evaluated from a given distribution of θ and ψ_g^* on a regular grid in GM space in the same way that the QG forcing F in (1) can be evaluated from a given distribution of θ and ψ_g on a regular grid in physical space.

In order for (7) to admit a unique solution the ellipticity condition $(fP)>0$ must be satisfied throughout the domain of integration. Furthermore, the GM transformation is only valid in the sense of providing a one-to-one mapping between physical and GM co-ordinates if J does not change sign anywhere within the domain of the transformation. In practice this means that both $(fP)>0$ *and* $J>0$ have to be satisfied everywhere within the domain of integration. The condition $(fP)<0$, $J>0$ can arise in a local region of absolute instability. In that case a solution may still be obtained by replacing each negative grid-point value of (fP) by some small positive

number $(fP)_{min}$ prior to numerical integration. However, no meaningful solution is possible if J is locally less than zero , since the GM transform is then no longer valid throughout the domain of the analysis.

If both (fP) and J are everywhere positive and F^* can be evaluated on a suitable grid in GM space, a solution for w^* can be obtained numerically using a similar techniques to that used to solve (1). Of course, this procedure implies the need for a transformation of the sampled fields from physical to GM co-ordinates, followed by a transformation of the solution back onto physical co-ordinates. The need for these transformations implies that a SG diagnosis of vertical velocity associated with a feature represented by gridded data in physical space is technically more involved than the QG diagnosis.

It is noted in HD that the derivation of (7) also requires that in (6) the non-linear terms in the expression for ζ_g^* be small relative to ζ_g (though Montgomery and Farrell (1992) have relaxed this requirement to yield an omega equation with extra terms on the right-hand-side involving time derivatives). However, it should be recognised that the GM co-ordinate transformation (4) has the full non-linear J as its Jacobian, irrespective of whether any approximations to J are assumed in deriving (7). It is therefore not clear whether solving (7) will lead to a realistic diagnosis of w when the condition $\zeta_g^* \approx \zeta_g$ is not actually satisfied. We postpone a discussion of this aspect of the problem to Part II.

3. Evaluation of the SG forcing of vertical velocity

In order to solve (7) by discrete integration, it is necessary to evaluate its various terms on a regular grid in GM space spanning the chosen 3-d domain of

integration. Of particular concern is the accurate representation of the SG forcing (F^*) considered as a function of location in GM space, which is implied by a given distribution of θ and ψ_g sampled at the nodes of a regular grid in physical space. Here we discuss this problem with particular reference to the analysis of data generated by a primitive equation (PE) model simulation of a baroclinic development in middle latitudes (see Appendix A).

General Principles

We assume that θ and pressure, and hence ψ_g, are known at the nodes of the model grid. It follows that we can proceed in one of two ways, summarised as follows:-

Method 1. At each level in the vertical, evaluate $\mathbf{V}_g$ and hence $\psi_g^* = \psi_g + \frac{1}{2f}\left(u_g^2 - v_g^2\right)$, on the model grid. Using the same values of $\mathbf{V}_g$, locate these data points in GM space by applying the GM co-ordinate transform (4) to the nodes of the model grid. (These locations will form an irregular grid in GM space.) Interpolate θ and ψ_g^* between the known data points to obtain values sampled at the nodes of a regular grid in GM space and hence evaluate F^* on the latter by standard centred-differencing methods applied to θ and ψ_g^* variables. This is the approach apparently used by Graham (1991) and Pinot et al. (1996).

Method 2. Evaluate $\mathbf{V}_g$, $\mathbf{Q}$ and J on the model grid, using centred differencing methods applied to the given values of θ and ψ_g. Given that $\mathbf{Q}^*=\mathbf{Q}/J$, hence evaluate F^* on the model grid with the aid of (5). Locate the sampled data points in GM space as in Method 1 and interpolate F^* between these points to obtain values sampled at the nodes of a regular grid in GM space.

In both methods, similar principles of course apply to the evaluation of P on the nodes of a regular grid in GM space: it can either be evaluated from interpolated values of θ and ψ_g^*, or evaluated on the model grid prior to the interpolation step.

In numerical terms, Method 1 is simpler, since it does not involve applying explicitly the relationship between differential operators defined by (5). However, it suffers from two disadvantages. The first is that the effect of interpolation errors on θ and ψ_g^* can be amplified substantially when differencing operators are applied to these grid point variables in GM space. As noted below, operations in GM space on a discrete field obtained by interpolating between the transformed data points are inevitably affected by aliasing errors resulting from the effect of scale distortion. This can result in relatively large errors on the output from differencing operators and their convolutions applied to the interpolated data, even following accurate interpolation. The problem is avoided using Method 2, since here all the differencing is carried out in the model space.

The second disadvantage with Method 1 is that there is no direct way of verifying the accuracy of the estimated forcing evaluated on the grid in GM space. On the other hand, it is a simple matter to apply an inverse transform to F^* estimated on the GM grid by Method 2 (see below), the result of which can then be compared with the values originally calculated on the model grid. Such a verification is clearly desirable in order to ensure that any differences between a SG diagnosis of vertical velocity and a QG (or alternative) diagnosis cannot be attributed simply to the estimation error on the interior distribution of the diagnosed forcing.

Given the required distribution of F^* and P in GM space (and subject to the condition $(fP)>0$), a numerical integration of (7) provides an estimate of w^* sampled

on the GM grid. Applying an inverse transform to these data and using $w=Jw^*$ then leads to the required solution for w sampled on the model grid. Actual solutions are discussed in Part II; here we focus on the transformation problem itself, with particular attention to the evaluation of the SG forcing and factors affecting its representation in GM space.

Evaluations on the model grid

Figure 1 shows the model-generated distribution of ψ_g and θ at a height of 500 m above the lower boundary, corresponding to day 7 of the model integration. At this time the model has developed an intense low-level cyclonic circulation with geostrophic absolute vorticity (ζ_g) of the order of $5f$ at its centre (marked L on the Fig. 1), decreasing to a minimum of the order of $0.6f$ some 500 km north of L. The Jacobian of the GM transform (J) within the dynamically most active region ranges from 8.9 near L to a minimum of 0.5 in the region where ζ_g is also a minimum (Fig. 2). The substantially larger range in J compared with its linear approximation (ζ_g/f) suggests that the contribution from the non-linear terms in (6) is significant. Nevertheless, the fact that J is everywhere greater than zero implies that a one-to-one mapping between physical and GM co-ordinates is theoretically possible throughout the domain of interest. (It is for this reason that we chose to focus on the day 7 results in this section; the problem of obtaining a SG diagnosis for a domain within which J is locally negative is considered in section 4.)

Figure 2 also shows the location of the nodes of the model grid in GM-space, i.e. following a GM transformation of co-ordinates using geostrophic velocities evaluated on the model grid. Notice the considerable 'expansion' of grid cells associated with the region where J is substantially greater than unity on the model

domain. Less obvious is a substantial 'contraction' of cells associated with regions of strong negative wind shear ($J<1$).

The QG forcing (F) evaluated on the model grid (Fig. 3) exhibits a classic dipole structure with centres of maximum forcing for ascent (Northeast of L) and maximum forcing for descent (south of L) separated by about 400 km. At this level F ranges from -1.9×10^{-15} $m^{-1}s^{-3}$ to $+1.7\times10^{-15}$ $m^{-1}s^{-3}$. Figure 4 shows the horizontal distribution of the SG forcing F^*, also evaluated on the model grid. Values range between -1.1×10^{-15} $m^{-1}s^{-3}$ and $+0.9\times10^{-15}$ $m^{-1}s^{-3}$, which is smaller than the range in F, possibly reflecting mainly the influence of the inverse J scaling in the relationship between $\mathbf{Q}$ and $\mathbf{Q}^*$, especially in the dynamically active region where J is substantially larger than unity. On the other hand F^* appears to contain more small-scale structure than F. It is clearly important that such detail is correctly represented in GM space if (7) is to yield a realistic solution for w^* which is consistent with the forcing evaluated on the model grid. It follows that careful consideration should be given to the accuracy of an interpolation used to effect the transformation between model and GM co-ordinates.

Forward and Inverse transformations

In the following, we let $\{\mathbf{r}\}_n$ (= $\{\mathbf{r}_i, i=1,2,....n\}$) denote an ordered sequence of n regular grid point locations in the model space, with $\mathbf{r}_i=(x_i, y_i)$. The sequence of collocated values of a given field $\phi(\mathbf{r})$ is represented by $\{\phi(\mathbf{r})\}_n$ (= $\{\phi(\mathbf{r}_i), i=1,2,....n\}$). Given the geostrophic velocity $\mathbf{V}_g$ evaluated at $\mathbf{r}_i$, the GM transform (4) associates with each grid-point in the model space a corresponding location in GM space, $\mathbf{R}_i$, so that

$$\{\phi(\mathbf{r})\}_n=\{\phi(\mathbf{R})\}_n \qquad (10)$$

in which $\phi(\mathbf{R}_I)=\phi(X_I,Y_I)=\phi(x_i,y_i)=\phi(\mathbf{r}_i)$.

The problem of the *forward transform* is defined by: given $\{\mathbf{V}_g(\mathbf{r})\}_n$ and $\{\phi(\mathbf{r})\}_n$, estimate $\phi(\mathbf{R})$ evaluated on a regular grid of M points in GM space. The required sequence is denoted by $\{\phi(\mathbf{R})\}_M$ $(=\{\phi(\mathbf{R}_J),\ J=1,2,....M\})$. A solution can be obtained from an interpolation of the form

$$\hat{\phi}(\mathbf{R}_J)=G_J\left(\{\phi(\mathbf{R})\}_n\right) \tag{11}$$

where $G_J\left(\{\varphi\}_n\right)$ represents the interpolating function (determined from the given data $\{\varphi\}_n$) evaluated at $\mathbf{R}_J$.

The problem of the *inverse transform* is defined by: given $\{\mathbf{V}_g(\mathbf{r})\}_n$ and $\{\phi(\mathbf{R})\}_M$ estimate $\{\phi(\mathbf{r})\}_n$. This can be solved using an interpolation of the form:

$$\hat{\phi}(\mathbf{r}_i)\equiv\hat{\phi}(\mathbf{R}_i)=G_i\left(\{\phi(\mathbf{R})\}_M\right) \tag{12}$$

where $G_i\left(\{\varphi\}_M\right)$ represents the interpolating function (determined from the given data $\{\varphi\}_M$) evaluated at $\mathbf{R}_i$. (Notice that in the case of the inverse transform it is not necessary to know $\mathbf{V}_g$ evaluated on the regular grid in GM space.)

Since here ϕ is only sampled on the nodes of the model grid, it is obviously not possible to determine the accuracy of the forward interpolation onto $\{\mathbf{R}\}_M$ using (11). However, it *is* possible to verify the result of (12) when $\{\phi(\mathbf{R})\}_M$ is replaced by $\left\{\hat{\phi}(\mathbf{R})\right\}_M$, i.e. when the inverse transform is applied to the result of the forward transform. The resulting sequence $\left\{\hat{\phi}(\mathbf{r})\right\}_n$ can then be compared with the original given sequence $\{\phi(\mathbf{r})\}_n$. Since this procedure involves two interpolations (one being

applied to the output of the other), the magnitude of the perceived error on the retrieved field $\hat{\phi}(\mathbf{r})$ is likely to be larger on average than the actual error on $\hat{\phi}(\mathbf{R})$. It is thus possible to infer at least an upper bound on the interpolation error following the forward transform, which can also be considered as representing an upper bound on the error associated with an inverse transform applied to a given field sampled in GM space.

Practical Solutions

It is possible to solve the forward interpolation (11) by choosing an interpolation scheme whose input parameters comprise the sampled values of a field considered as a function of co-ordinate variables in GM space. Such a scheme thus takes data from an irregular grid (as in Fig. 2) and interpolates directly onto a regular grid. In the following we refer to a transform based on this principle as *direct*. Figure 5 shows the result of applying a direct interpolation method (using the scheme developed by Franke and Nielson (1980)) to potential temperature and SG forcing data sampled on commensurate grids in model and GM spaces (compare with Fig. 4). It is clear that an accumulation of error during either or both of the forward and inverse interpolations results in a rather poor retrieval of $F^*(\mathbf{r})$ in some regions. We later demonstrate that a more accurate retrieval can only be achieved if the grid point resolution used to represent $F^*(\mathbf{R})$ on the GM grid is chosen to be substantially greater than that of the model grid. Unfortunately, this incurs a large numerical penalty in the case of direct transform methods, especially when interpolating from GM to model co-ordinates.

An alternative approach, along the lines of that used by Graham (1991), is to replace (11) by

$$\hat{\phi}(\hat{\mathbf{r}}_J) = G_J\left(\{\phi(\mathbf{r})\}_n\right) \tag{13}$$

where $\hat{\mathbf{r}}_J$ is the estimated location of a point in the model space associated with the required grid point $\mathbf{R}_J$ in GM-space. In the following we refer to a transform based on this principle as *indirect*. The advantage is that the input parameters for the interpolation now comprise the data sequence $\{\phi(\mathbf{r})\}_n$ sampled on the regular grid in model space, and the numerical problem of interpolating between points in a large two-dimensional array is greatly simplified. Furthermore, interpolation accuracy does not then depend on the influence of the co-ordinate transform on the local distribution of data points in GM space, which can otherwise influence the accuracy of an interpolation between irregularly spaced data points.

A preliminary estimate of $\hat{\mathbf{r}}_J$ in (13) can be obtained by assuming a linear approximation to $\mathbf{V}_g(\mathbf{r})$ between the vertices of triangular cells in physical space, following a triangular tessellation of the model grid (Fig. 6). This assumption implies that a GM transform applied to all points on the boundary of one such cell generates an associated triangular cell in GM space, within which $\mathbf{V}_g$ also varies linearly with respect to the GM co-ordinate variables X and Y. If the required point (X_J, Y_J) is known to lie within one such triangle in GM space, then the value of $\mathbf{V}_g$ at that point can be estimated by simply interpolating linearly with respect to X and Y between its vertices to obtain $\hat{u}_g(R_J), \hat{v}_g(R_J)$, and the point $\hat{\mathbf{r}}_J = (\hat{x}_J, \hat{y}_J)$ subsequently determined from the inverse co-ordinate transform

$$\begin{aligned} \hat{x}_J &= X_J - \hat{v}_g(\mathbf{R}_J)/f \\ \hat{y}_J &= Y_J + \hat{u}_g(\mathbf{R}_J)/f \end{aligned} \tag{14}$$

As noted by Graham (1991), a linear interpolation of geostrophic velocity components can result in significant errors on $\hat{\mathbf{r}}_J$ in regions of rapidly varying shear or curvature in the geostrophic wind field. However, following the principle introduced by Schär and Davies (1990), a more accurate solution can be obtained by iteration. Thus following the k'th iteration we estimate a new value of $\hat{\mathbf{r}}_J$ as

$$\hat{\mathbf{r}}_J[k+1] = \mathbf{R}_J + \frac{1}{f}\mathbf{k} \times \hat{\mathbf{V}}_g[k] \tag{15a}$$

and subsequently up-date the estimate of velocity at $\mathbf{R}_J$ using

$$\hat{\mathbf{V}}_g[k+1] = \beta \hat{\mathbf{V}}_g[k] + (1-\beta)\hat{\mathbf{V}}_g(\hat{\mathbf{r}}_J[k+1]) \tag{15b}$$

where β (=0.4 in this study) is a weighting factor chosen to ensure stable convergence. The scheme is initialised using the value of $\hat{\mathbf{V}}_g$ obtained by linear interpolation onto $\mathbf{R}_J$ in GM space, so that for k=0 (15a) is equivalent to (14). However, in (15b) $\hat{\mathbf{V}}_g(\hat{\mathbf{r}}_J[k+1])$ represents an estimate of $\mathbf{V}_g(\mathbf{R}_J)$ using the higher-order interpolation scheme applied in model space. The method is considered to have converged when the absolute difference between the components of $\hat{\mathbf{V}}_g(\hat{\mathbf{r}}_J[k+1])$ and $\hat{\mathbf{V}}_g[k]$ are both less than some prescribed upper limit (0.1 m s^{-1} in this study).

Figure 7a shows the retrieved potential temperature and SG forcing which result from applying the indirect method to these variables sampled on commensurate grids in model and GM spaces, using a bi-cubic spline as the interpolating function required to estimate $\mathbf{V}_g(\mathbf{R}_J)$ and to solve (12) in the inverse transform. Results are comparable to those obtained using the direct method, though errors on retrieved variables are slightly reduced (see first two rows of tables 1 and 2). For comparison, Fig. 7b shows the result of using the indirect method in an analysis based on evaluating

F^* in GM space from an interpolated field of ψ_g^* (as in Method 1 under *General Principles).* This approach is substantially less accurate (rms error = 1.2×10^{-16} $m^{-1}s^{-3}$) than either the direct or indirect method applied to F^* evaluated on the model grid.

The resolution problem

One obvious result of the GM transform is a compression of horizontal scale in regions where J is significantly less than unity, which in model space generally corresponds to $(\xi_g / f) < 1$. The effect is illustrated schematically in Fig. 8, which represents the purely one-dimensional case where $\mathbf{V}_g(\mathbf{r}) = (0, v_g(x))$ and $\phi(\mathbf{r}) = \phi(x)$. The result is that the spectral distribution of $\phi(X)$ contains contributions from higher wavenumber components than those representable on the discrete grid in the model space. This implies that an interpolation onto a grid in GM space which has the same sampling interval as the grid in the model space will generate a discrete field whose spectral representation may contain substantial aliasing errors. Such errors are of no consequence in relation to the accuracy of individual values of $\hat{\phi}(X)$ sampled on $\{\mathbf{R}\}_M$. However, they *do* imply errors on the output of any linear operator acting on $\{\hat{\phi}(\mathbf{R})\}_M$, including, of course, the solution of (7) via numerical (discrete) integration of $F^*(\mathbf{R})$ sampled on the regular grid in GM space and the inverse transformation operator represented by (12). In the context of SG analysis the effect may be particularly serious due to the tendency for the forcing pattern in GM space to contain substantial contributions from spatial features whose scales are substantially smaller than those characterising $F^*(\mathbf{r})$ (see below).

The only method that can be guaranteed to reduce the effect of aliasing error, is to interpolate (either directly or indirectly) onto a grid in GM space which has a higher

resolution than the grid in the original model space. The required sampling interval can in principle be related to the minimum of J sampled on $\{\mathbf{r}\}_n$, since $J(\mathbf{r}_i)$ measures the fractional change in area (and hence scale) of an elementary local region surrounding a point $\mathbf{r}_i$ following a GM transform applied to the points on its boundaries. In the 1-d case illustrated in Fig. 8, $J=(1+a)$, where $a=(1/f)\partial v_g/\partial x$, and the fractional change in the distance between points along x is simply $(1+a)$. Hence if Δ_x is the given sampling interval in the model space, then the sampling interval in GM space which should provide the same degree of feature resolution is predicted by $\Delta_X=\min(1+a_i)\times\Delta_x$, where $\min(1+a_i)$ is the smallest value of $(1+a)$ sampled on $\{x\}_n$.

In the 2-d case the relationship between sampling interval and J is more complicated, due to the deformation of local regions associated with the 'stretching' component b (see under (5)). If the latter is ignored, then suitable sampling intervals for a regular grid in GM space might be estimated using $\Delta_R \approx \min\left((1+a_i),(1+c_i)\right)\times\Delta_r$, where Δ_r is the sampling interval on the model grid. For the simulated data being considered here, such a rule suggests a value of Δ_R which is about one third of Δ_r (i.e. ~30 km). Although such a rule may provide useful guidance, there is theoretically no good reason for ignoring the contribution from the stretching term, in which case it may be difficult to predict a suitable sampling interval directly from the measured values of J.

An alternative more empirical approach is to choose a sampling interval which results in an accurate retrieval of $\{\phi(\mathbf{r})\}_n$ when an inverse transform is applied to the output of the forward transform evaluated on the chosen GM grid $\{\mathbf{R}\}_M$. For a given interpolation scheme, the accuracy of such a retrieval should depend only on the input

information content of the discrete data sampled in GM-space, which for a given field depends only on M (subject to the condition that $\{\mathbf{R}\}_M$ spans a region whose boundaries do not vary with M).

The effect of increasing resolution in GM space on the accuracy of θ and F^* retrievals is summarised in Tables 1 and 2. Within the domain of interest, increasing resolution by a factor of four reduces both extreme and rms errors by the order of ×50. The retrieved fields based on the indirect interpolation method with this GM space resolution are shown in fig. 9 (compare with Fig. 4). It is clear that a 25 km resolution in GM space is sufficient to reduce the forward interpolation error to a level which can be considered negligible compared with the actual range of sampled variation (the order of 30 K in the case of θ and 2×10^{-15} $m^{-1}s^{-3}$ in the case of F^*).

The reason why a high grid-point resolution in GM space is so beneficial becomes rather obvious when we examine the representation of θ and F^* in GM space (Fig. 10). In the case of F^*, regions enclosing extrema tend to coincide with regions where J is less than unity , implying a compression of horizontal scale under a GM transform (compare with Fig. 4). The effect is particularly noticeable in the region of the main forcing dipole Northeast of **L**, where the separation between extrema in $F^*(\mathbf{R})$ is only of the order of 100 km, in contrast to a separation scale of the order of 400 km associated with extrema in $F^*(\mathbf{r})$. The effect is less marked in the case of the potential temperature field. Nevertheless, the higher resolution appears to be essential in order to resolve accurately the large variations in horizontal temperature gradient depicted by the GM space representation of the cyclone.

It is important to note that employing a higher resolution grid to evaluate $F^*(\mathbf{R})$ from interpolated $\psi_g^*(\mathbf{R})$ data (see Method 1 under *General Principles*) does

not generally result in a more accurate representation of the forcing: the problem with this approach is that the reduced differencing scale results in increased amplification of interpolation errors on $\psi_g^*(\mathbf{R})$ This more than offsets any potential improvement associated with better resolution of features in regions where J is small. For the case considered here we have found that the effect of increasing resolution was to generate highly unrealistic extremes in the estimated forcing following the application of either the direct or indirect approach to transforming between model and GM gridded data.

4. Approximations when J is not everywhere positive

Figure 11 shows the simulated fields of ψ_g and θ at day 8 of the model intergration, again at a height of 1000 m above the lower boundary. At this mature stage of development the horizontal circulation is extremely intense, with ζ_g ranging from - 0.2f to + 6f over the model domain. At the same level, the cyclone-scale QG forcing pattern (Fig. 12) is somewhat weaker than at day 7. On the other hand, a significant frontal-scale signature is apparent to the west and south of **L**.

In contrast to day 7, the distribution of J calculated from the grid point velocities indicates that there is a substantial region around the periphery of the main cyclone at day 8 within which J is less than or equal to zero (Fig. 13). This not only implies that the condition $(fP)>0$ is violated (assuming, as is actually the case, that $\partial\theta/\partial Z$ is generally positive), but also that there is no unique 'one-to-one' mapping between model and GM co-ordinates throughout the domain of interest. In effect we can say that for this case $\{\psi_g(\mathbf{r})\}_n$ lies outside the discrete phase space within which SG theory is applicable and there is therefore no way we can approximate the model generated vertical velocity w by a SG diagnosis derived from the PE model data.

Paradoxically, such a difficulty is not apparent as far as the applicability of QG theory is concerned, provided $\overline{N^2}(z)>0$ for all z: this is sufficient to guarantee that (1) is elliptic and therefore admits a solution for w subject to the specification of appropriate boundary conditions. Thus, regardless of whether or not the approximations assumed in deriving (1) are satisfied, a QG solution for w is at least *technically* possible given $\overline{N^2}(z)>0$, whereas the same situation does not necessarily apply in the case of a SG solution.

The above considerations suggest that the only way in which we can apply (7) in practice is to replace $\{\psi_g(\mathbf{r})\}_n$ at each model level by some approximation $\left\{\tilde{\psi}_g(\mathbf{r})\right\}_n$ so that the associated values of J on $\{\mathbf{r}\}_n$ are everywhere greater than some small positive constant J_{min}. Graham (1991) was able to obtain such an approximation by applying a smoothing filter to the grid point data corresponding to a real data case for which J was initially less than zero at some locations within the analysis domain. However, such an approach is less successful when applied to the data structure represented in Fig. 11: here the degree of spatial filtering required to result in $J>0$ everywhere is so great that most of the sub-cyclone scale structure is removed, effectively undermining the potential advantage of any subsequent SG analysis to represent ageostrophic circulation features which might be poorly resolved by a QG analysis in regions of large PV anomaly.

An alternative approach is to apply an adjustment to $\{\psi_g(\mathbf{r})\}_n$ which affects mainly those regions where J is initially negative but which has little impact on the geopotential structure elsewhere. At a single height level this can be achieved by seeking a solution $\left\{\tilde{\psi}_g\right\}_n \leftrightarrow \left\{\tilde{J}\right\}_n$ which satisfies

$$\begin{aligned} \tilde{J}_i &= J_i \quad , \quad J_i \geq J_{\min} \\ &= J_{\min} \quad , \quad J_i < J_{\min} \end{aligned} \tag{16}$$

where J_i is the initial value of J at a grid-point and $J_{\min}$ is a prescribed lower limit on J. (A method of solution is given in Appendix B). Applying such an adjustment only at those height levels where J is initially less than $J_{\min}$ implies that the temperature distribution is also adjusted, which could give rise to unrealistic (even negative) values of N^2. This problem is avoided if the increments added to $\{\psi_g(\mathbf{r})\}_n$ so as to result in $J>J_{\min}$ everywhere at one level are also added at all other levels. It follows that more than one adjustment at each level may be required before (16) is satisfied simultaneously at all levels.

Figure 14 illustrates the effect of applying such an adjustment scheme to the day-8 ψ_g data for a prescribed value of $J_{\min}$ equal to 0.3. The method results in a relatively large adjustment to $\psi_g(\mathbf{r})$ near where J was originally much less than zero, but only small (mainly negative) changes elsewhere. Furthermore, the adjustment retains most of the detail in the strongly cyclonic regions near the centre (L) and within the 'frontal' band to the east of L (compare Figs 15 and 12). The QG forcing field calculated from the adjusted data (Fig. 16) closely resembles that calculated from the original data (Fig. 12), which suggests that the adjusted structure can also be considered as a close 'dynamical' approximation to the model generated circulation. Figure 17 shows the corresponding distribution of F^* evaluated on the model grid. The influence of the inverse J scaling on the relationship between F and F^* becomes particularly apparent around the periphery of the cyclonic circulation, where J is substantially less than one. In those regions the magnitude of extrema in F^* are typically four times greater than the associated extrema in F. Very large values of

geostrophic shear also results in an even greater degree of scale distortion by the GM transform than was apparent at day 7. Some impression of this effect is given by Fig. 18, which shows the result of an interpolation of $F^*(\mathbf{R})$ onto a GM grid spanning the full 4000 km × 4000 km domain. Figure 18b shows detail of the sampled structure within a sub-domain measuring 1600 km × 1600 km (see inset on Fig. 18a), derived from forward interpolations of θ and F^* onto a 12.5 km resolution grid in GM space. The converging strips of strong positive forcing can be seen to relate to two areas of positive QG forcing (for descent) on either side of the thermal ridge in the Southwest sector of the model domain (Fig. 16). However, the influence of strong negative geostrophic shear in this region has lead to a remarkable degree of scale compression, such that the separation between F^* extrema in GM space is typically less than 200 km, compared with about 2000 km separating the associated F extrema in model space.

The presence of regions of strong negative geostrophic shear implies that a very high grid-point resolution in GM space may be required in order to capture all those significant features of the semi-geostrophic forcing which can be diagnosed from ψ_g,θ data sampled on the model grid (see section 4). The problem is illustrated by the retrieval error statistics shown in Table 3, which result from analysis of the day-8 model data following adjustment of $\psi_g(\mathbf{r})$ using various values of J_{min}. For a given grid-point resolution in GM space, retrieval errors increases dramatically for $J_{min}<0.5$. These results imply that it may be very difficult to apply SG analysis methods in practice to intense circulation features that include regions of large anticyclonic shear.

5. Conclusions

The diagnosis of vertical velocity via a solution of the semigeostrophic (SG) omega equation is theoretically no more difficult than a diagnosis via a solution of the quasigeostrophic (QG) omega equation. However, there are some technical difficulties in deriving an accurate representation of the SG forcing on geostrophic momentum co-ordinates when the given geopotential and temperature distribution is sampled on a conventional physical co-ordinate system. A simple 'indirect' approach to the forward transform problem can provide an accurate representation of the required forcing on a regular grid in GM space, given values of the SG forcing evaluated on a regular grid in physical space. However, the sampling density in GM space may need to be considerably greater than in physical space in order to capture all those spatial features which are resolved on the physical grid.

A GM transform of co-ordinates is only meaningful if the Jacobian of the transformation (J) is everywhere positive within the region of interest. Otherwise, it is not possible to diagnose the observed circulation under SG theory. On the other hand, it is possible to apply a variational adjustment to the observed distribution of geopotential so that the resulting field of J has some prescribed positive lower bound, without greatly affecting the original distribution where J was significantly greater than zero. In this way it may be possible to define a semigeostrophic attribution for features which do not posses a unique representation in GM space.

Acknowledgement

The authors wish to thank Brian Hoskins for helpful comments relating to theoretical aspects of this study.

APPENDIX A

PE model solutions

Here and in Part II the database used to test diagnostic analysis methods is taken from a simulation of an idealised baroclinic wave life-cycle using a hydrostatic Boussinesq numerical model (Rotunno et al., 1994). The simulation is initialised with a zonal jet associated with a sharply sloping tropopause in the middle of a meridional channel. The model troposphere and stratosphere have different but constant potential vorticities. In the zonal direction the model is periodic (4000 km domain) and is a closed channel (width equal to 8000 km) in the meridional direction. The model resolution is 100 km in the horizontal and 250 m in the vertical, with a vertical extent of 15 km. A perturbation is introduced to initialise cyclogenesis and by day 7 a well-developed, mature cyclone has evolved. Although the idealisation involves a representation only of dry adiabatic and frictionless motion, the model nevertheless represents a complete and essentially realistic manifestation of an extra-tropical cyclone.

The model output consists of grid-point values of horizontal and vertical wind components, potential temperature, pressure and potential vorticity. For the purposes of this study, a simple moving average filter was applied to all the model generated fields in order to remove what were considered to be unrealistic grid-scale features prior to any diagnostic analysis. Differencing and quadrature operators were applied over the full model domain, though only results for the central 4000 km × 4000 km region are shown on most of the Figures in the main text.

APPENDIX B

Adjusting a geostrophic streamfunction field to satisfy $J>J_{min}$

Let $\underline{\psi}_g$ be an N-vector of geostrophic streamfunction values sampled on a horizontal grid, and $\underline{J}$ the associated vector of values of the Jacobian of the GM transformation evaluated on the same grid. We seek some 'minimal' adjustment to $\underline{\psi}_g$ so that the values of J calculated from the new vector $\underline{\tilde{\psi}}_g$ satisfy (16). An appropriate solution is one which minimises the mean square adjustment subject to the requirement that $\underline{\tilde{\psi}}_g$ satifies the set of N strong constraints $J_i\left(\underline{\tilde{\psi}}_g\right)-\tilde{J}_i=0, i=1,2,\ldots,N$. An approximate solution can be found using an iterative descent algorithm based on Newton's method (Beale, 1988). Thus following k iterations the estimate of $\tilde{\psi}_g$ is calculated from

$$\hat{\underline{\tilde{\psi}}}_g[k+1]=\hat{\underline{\tilde{\psi}}}_g[k]-(\mathbf{A}_k+\mathbf{I}\lambda_k)^{-1}\left(\hat{\underline{J}}[k]-\underline{\tilde{J}}\right) \qquad \text{(B1)}$$

Here $\mathbf{A}_k$ is a matrix of partial derivatives with *i,j'th* entry given by

$$\left(a_{ij}\right)_k=\frac{\partial\hat{\tilde{J}}_i[k]}{\partial\hat{\tilde{\psi}}_{gj}[k]},$$

$\mathbf{I}$ is the unit matrix and λ_k (≥ 0) a scalar chosen to make $(\mathbf{A}_k+\mathbf{I}\lambda_k)$ positive definite. The method is initialised by setting $\hat{\underline{\tilde{\psi}}}_g[0]=\underline{\psi}_g$ and is considered to have converged to the required solution once $\hat{\tilde{J}}[k]$ everywhere exceeds J_{min}-ε, where ε is a positive constant $<<J_{min}$. If J_i is calculated by conventional centred differencing on a 3×3 stencil, then $(\mathbf{A}_k+\mathbf{I}\lambda_k)$ can be written in the form of a sparse symmetric band matrix

containing (p+1) sub-diagonals, where p is the number of grid-points measured along one of the co-ordinate directions on the given grid. The required inverse is then easily obtained using a Cholesky factorisation, which exploits these sparse symmetric properties (Wilkinson and Reinsch, 1971).

The above method does not necessarily provide an acceptably 'smooth' solution for $\{\tilde{\psi}_g(\mathbf{r})\}_n$ in regions where the original value of (J-J_{min}) changes sign. However, that problem is easily overcome by applying a simple smoothing (e.g. order-1 moving-average) filter to the J increments in (B1) before each iteration. The result is to generate a 'smoother' adjustment that extends somewhat beyond the region where J was originally less than J_{min} (see Figs 14 and 15 in main text).

REFERENCES

Beale, E.M.L 1988 *Introduction to optimization.* Wiley, 121 pp.

Bluestein, H.B. 1992 *Synoptic-Dynamic Meteorology in Midlatitudes. Vol. 1: Principles of Kinematics & Dynamics.* Oxford University Press, 432 pp.

Bosart, L.F. and Lin, S.C. 1984 A diagnostic analysis of the President's day storm of February 1979. *Mon. Weather Rev.,* **112,** 2148-2177.

Carlson, T.N. 1991 *Mid-Latitude Weather Systems.* Harper Collins, 507 pp.

Franke, R. and Nielson, G. 1980 Smooth Interpolation of Large Sets of Scattered Data. *Int. J. Numer. Methods Engrg.,* **15,** 1691-1704.

Graham, R.J. 1991 *Diagnosis of mid-latitude synoptic development: a review, and a case study of a developing cyclone.* PhD Thesis, University of Edinburgh, 251 pp.

Holton, J.R. 1972 *An Introduction to Dynamic Meteorology.* Academic Press, 319 pp.

Hoskins, B.J. 1975 The geostrophic momentum approximation and the semigeostrophic equations. *J. Atmos. Sci.,***32,** 233-242.

Hoskins, B.J. and Draghici, I. 1977 The forcing of ageostrophic motion according to the semigeostrophic equations and in an isentropic coordinate model. *J. Atmos. Sci.*, **34,** 1859-1867.

Montgomery, M.T. and Farrell, B.F. 1992 Polar low dynamics. *J. Atmos. Sci,* **49,** 2484-2505.

Pinot, J-M., Tintoré, J., and Dong-Ping Wang. 1996 A study of the omega equation for diagnosing vertical motions at ocean fronts. *J. Marine Res.*, **54,** 239-259.

Räisänen, J. 1995 Factors Affecting Synoptic-Scale Vertical Motions: A Statistical Study Using a Generalized Omega Equation. *Mon. Weather. Rev.*, **123,** 2447-2460.

Rotunno, R., Skamarock, W.C., and Snyder, C. 1994 An analysis of frontogenesis in Numerical Simulations of baroclinic waves. *J. Atmos. Sci.*, **51,** 3373-3398.

Schär, C. and Davies, H.C. 1990 An Instability of Mature Cold Fronts, *J.Atmos. Sci.*, **47,** 929-950.

Wilkinson, J.H. and Reinsch, C. 1971 *Handbook for Automatic Computation (Vol.II, Linear Algebra).* Springer-Verlag, 431 pp.

TABLES

Method	Δ (km)	Lower bound (K)	Upper bound (K)	rms (K)
Direct	100	-0.73	+0.47	0.078
Indirect	100	-0.50	+0.53	0.051
Indirect	50	-0.08	+0.12	0.009
Indirect	25	-0.01	+0.007	0.0008
Indirect	12.5	-0.002	+0.002	0.0002

Table 1. Errors on retrieved potential temperature (θ) evaluated on the 2400 by 2400 km sub-domain shown on fig.1, using various grid-point resolutions (Δ) in GM space. Columns 3 and 4 show the extremes on perceived error. Column 4 gives the rms perceived error evaluated on the 576 grid points within the model sub-domain.

Method	Δ (km)	Lower bound ($10^{-16}m^{-1}s^{-3}$)	Upper bound ($10^{16}m^{-1}s^{-3}$)	Rms ($10^{16}m^{-1}s^{-3}$)
Direct	100	-5.5	+10.6	0.75
Indirect	100	-6.8	+7.5	0.72
Indirect	50	-2.2	+1.5	0.18
Indirect	25	-0.17	+0.17	0.018
Indirect	12.5	-0.04	+0.04	0.003

Table 2. Errors on retrieved SG forcing (F^*) evaluated on the 2400 by 2400 km sub-domain shown on fig. 1. Other details as in table 1.

Δ (km)	J_{min}=0.15	J_{min}=0.30	J_{min}=0.60
100	**44.8** *(127)*	**9.3** *(77)*	**1.5** *(0.55)*
50	**34.9** *(77)*	**6.6** *(39)*	**0.65** *(0.1)*
25	**25.0** *(40)*	**2.3** *(5)*	**0.055** *(<0.1)*
12.5	**9.2** *(5)*	**0.41** *(0.1)*	**0.0082** *(<0.1)*

Table 3. Errors on retrieved SG forcing F^* data evaluated on a 2400 km by 2400 km sub-domain following analysis of adjusted day-8 pressure data on the model grid, using various resolutions (Δ) in GM space. Numbers in bold type are rms grid-point errors in units of 10^{-16} m^{-1} s^{-3}. Numbers in parentheses correspond to the mean square error expressed as a fraction (in %) of the sample variance of F^* (calculated on the model grid). J_{min} is the minimum value of the Jacobian of the GM co-ordinate transformation within the model domain, following adjustment of the model pressure field data.

FIGURE CAPTIONS

Fig. 1 Geostrophic streamfunction (continuous contours drawn every 3×10^6 $m^2\ s^{-1}$) and potential temperature (dashed contours labelled in units of degrees *K*) on model level 3 (z=500 m) at day 7 of the model integration. The domain of the figure measures 4000 *km* by 4000 *km*. The inner square identifies an inner region measuring 2400 *km* by 2400 *km*, as represented on subsequent figures.

Fig. 2 Jacobian of the horizontal GM co-ordinate transformation within the inner region shown in Fig. 1. Contouring is in intervals of 1 for $J\geq1$ (continuous; with labels) and in intervals of 0.1 for $J<1$ (dashed; no labels). Also shown are geostrophic wind vectors (maximum length equivalent to 42 m s^{-1}) plotted at the model grid points, and the locations of the model grid points in GM space (as dots).

Fig. 3 QG forcing (continuous contours labelled in units of $10^{-16}\ m^{-1}\ s^{-3}$) and Q-vectors (maximum length equivalent to $2.0\times10^{-10}\ s^{-3}$) evaluated on the model grid within the inner domain shown in Fig.1. Potential temperature also shown by dashed contours (at intervals of 3 *K*).

Fig. 4 SG forcing (continuous contours labelled in units of $10^{-16}\ m^{-1}\ s^{-3}$) and Q*-vectors (maximum length equivalent to $1.3\times10^{-10}\ s^{-3}$) evaluated on the model grid. Other details as in Fig. 3.

Fig. 5 Retrieval of **Q***-vectors, SG forcing and potential temperature fields following forward and inverse GM transforms using a direct interpolation method. Plotting conventions as in Fig. 4.

Fig. 6 A schematic representation of a GM co-ordinate transformation applied to a triangular local region (abc) in physical space, which generates a triangular local region (ABC) in GM space, subject to the assumption that the geostrophic velocity components vary linearly between the vertices of (abc). This assumption also implies that any point G which is interior to (ABC) must map onto a point which is interior to (abc) under an inverse co-ordinate transform and that the geostrophic velocity components in GM space vary linearly between the vertices of (ABC).

Fig. 7 Retrievals following forward and inverse GM transforms using an indirect interpolation method. a) Forward and inverse transforms applied to **Q***-vectors and SG forcing evaluated in model space; b) Forward transform applied to SG streamfunction ψ_g^* evaluated on the model grid, followed by inverse transform applied to **Q***-vectors and SG forcing evaluated on the GM grid from interpolated values of ψ_g^*. Other details as in Fig. 4.

Fig. 8 One dimensional illustration of the scale-distortion effect of a GM co-ordinate transformation. In the upper panel (a), the continuous line represents a sinusoidal field sampled on the physical domain; the dashed line corresponds to the Jacobian of the horizontal transformation J $(=1+(1/f)\partial v_g/\partial x)$ associated with a sinusoidal variation in v_g along the x-direction. The lower panel (b) represents the

structure of the field and the Jacobian of the GM co-ordinate transformation as seen in GM space.

Fig. 9 Retrieval of **Q***-vectors, SG forcing and potential temperature fields following forward and inverse GM transforms using indirect interpolation method when the grid spacing in GM space (25 km) is one quarter of that in model space (100 *km*). Plotting conventions as in Fig. 4.

Fig. 10. SG forcing (continuous contours labelled in units of 10^{-16} m^{-1} s^{-3}) and potential temperature (dashed contours drawn at intervals of 3 K) on the GM co-ordinate domain (inner 2400 *km* by 2400 *km*), estimated using the indirect transform method with Δ_R=25 *km*. Also shown are **Q*** vectors plotted every 100 *km*.

Fig. 11 Geostrophic streamfunction (continuous contours drawn every 3×10^6 m^2 s^{-1}) and potential temperature (dashed contours labelled in units of degrees *K*) at day 8 of model integration. Other details as in Fig. 1.

Fig. 12 QG forcing (continuous contours labelled in units of 10^{-16} m^{-1} s^{-3}) and **Q**-vectors (maximum length equivalent to 2.6×10^{-10} s^{-3}) evaluated on the model grid within the inner domain shown in Fig. 11. Potential temperature also shown by dashed contours (every 3 *K*).

Fig. 13 Jacobian of the horizontal GM co-ordinate transformation within the inner region shown in Fig. 11. Contouring is in intervals of 1 with zero line marked

bold. Also shown are geostrophic wind vectors (maximum length equivalent to 80 $m\,s^{-1}$) plotted at the model grid points.

Fig. 14 Result of applying adjustment scheme to the day 8 model data so that J everywhere exceeds a minimum value of 0.3. Adjusted ψ_g field represented by continuous contours (every $3\times10^6\ m^2\ s^{-1}$); difference between adjusted and original field shown by dashed contours (labelled in units of $10^6\ m^2\ s^{-1}$. The domain of the figure is as in Fig. 1.

Fig. 15 Jacobian of the horizontal GM co-ordinate transformation within the inner region shown in Fig. 11, following adjustment. Other details as in Fig. 13.

Fig. 16 QG forcing, **Q**-vectors and potential temperature evaluated on the model grid following adjustment. Other details as in Fig. 12.

Fig. 17 SG forcing, **Q***-vectors and potential temperature evaluated on the model grid following adjustment. Other details as in Fig. 12.

Fig. 18 SG forcing (continuous contours) and potential temperature (dashed contours) in GM space, based on forward interpolation of adjusted day 8 data by indirect method onto a 12.5 *km* resolution grid. a) 4000 *km* by 4000 *km* domain (F^* contoured every $1\times10^{-15}\ m^{-1}\ s^{-3}$); b) 1600 *km* by 1600 *km* inner domain, as identified in panel a) (F^* contoured every $5\times10^{-16}\ m^{-1}\ s^{-3}$). θ contours drawn every 3 K in both panels.

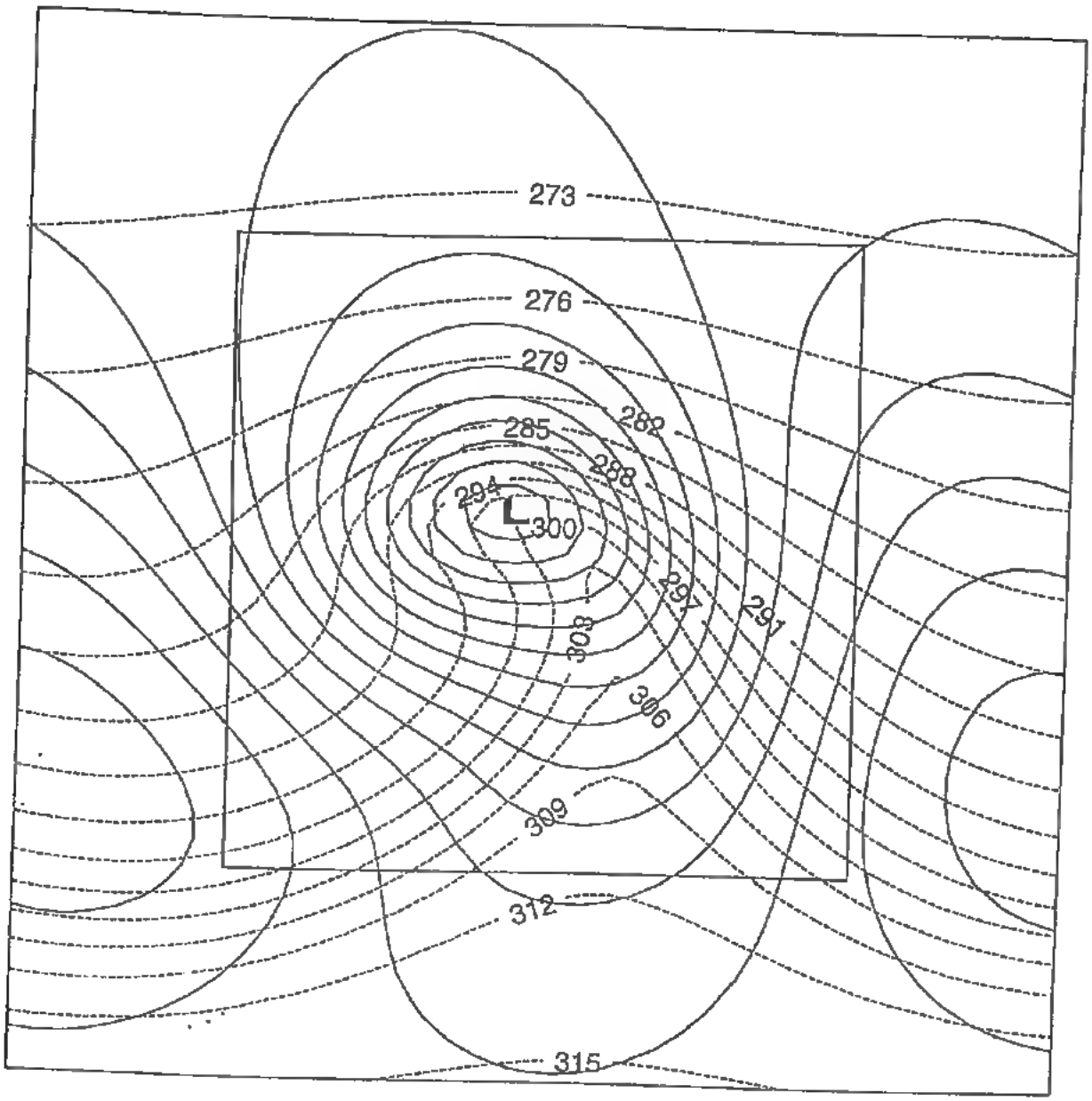

Fig. 1 Geostrophic streamfunction (continuous contours drawn every 3×10^6 $m^2\ s^{-1}$) and potential temperature (dashed contours labelled in units of degrees *K*) at day 7 of model integration. The domain of the figure measures 4000 *km* by 4000 *km*. The inner square identifies an inner region measuring 2400 *km* by 2400 *km*, as represented on subsequent figures.

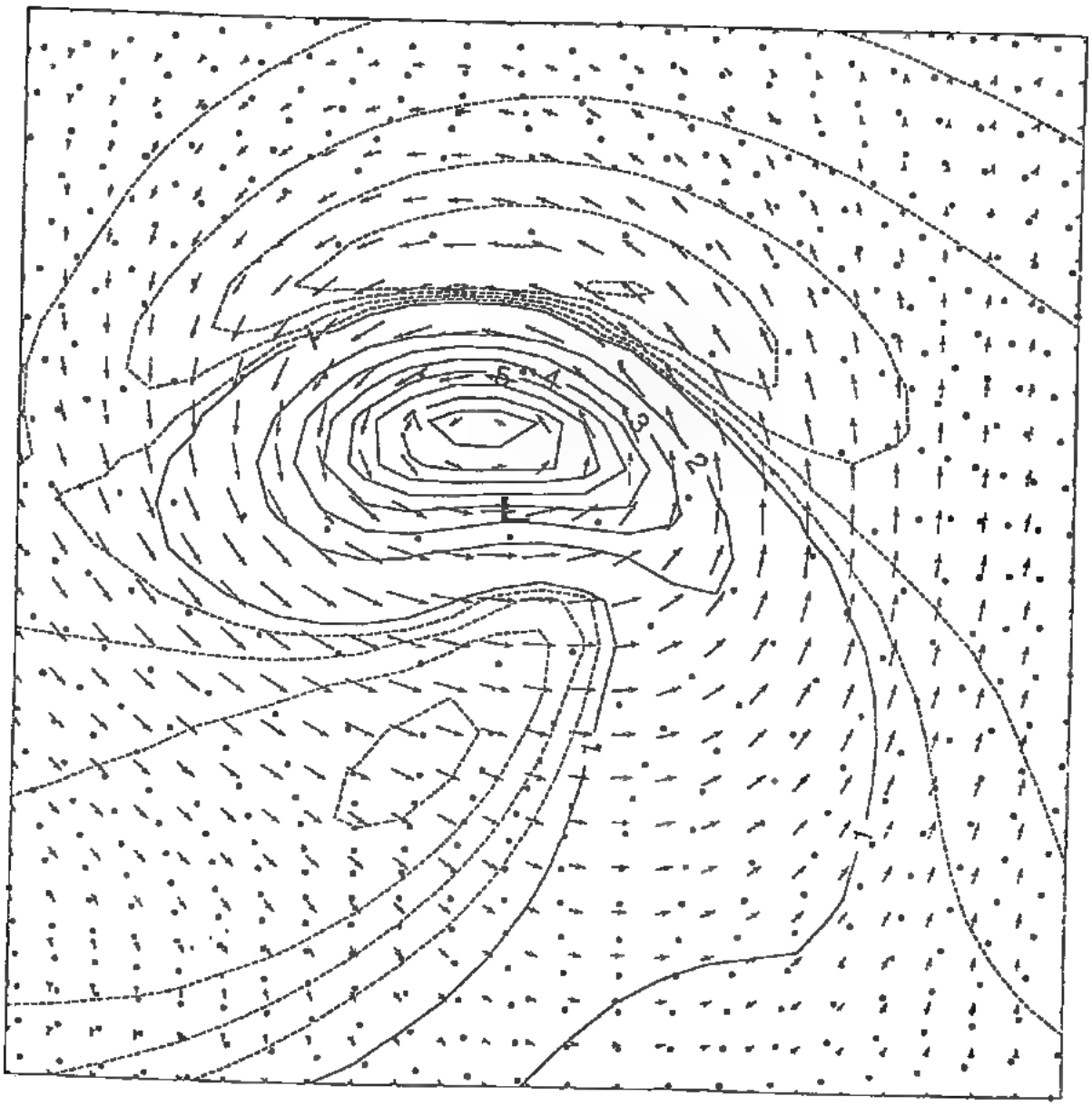

Fig. 2 Jacobian of the horizontal GM coordinate transformation within the inner region shown in Fig. 1. Contouring is in intervals of 1 for $J \geq 1$ (continuous; with labels) and in intervals of 0.1 for $J < 1$ (dashed; no labels). Also shown are geostrophic wind vectors (maximum length equivalent to 42 m s^{-1}) plotted at the model grid points, and the locations of the model grid points in GM space (as dots).

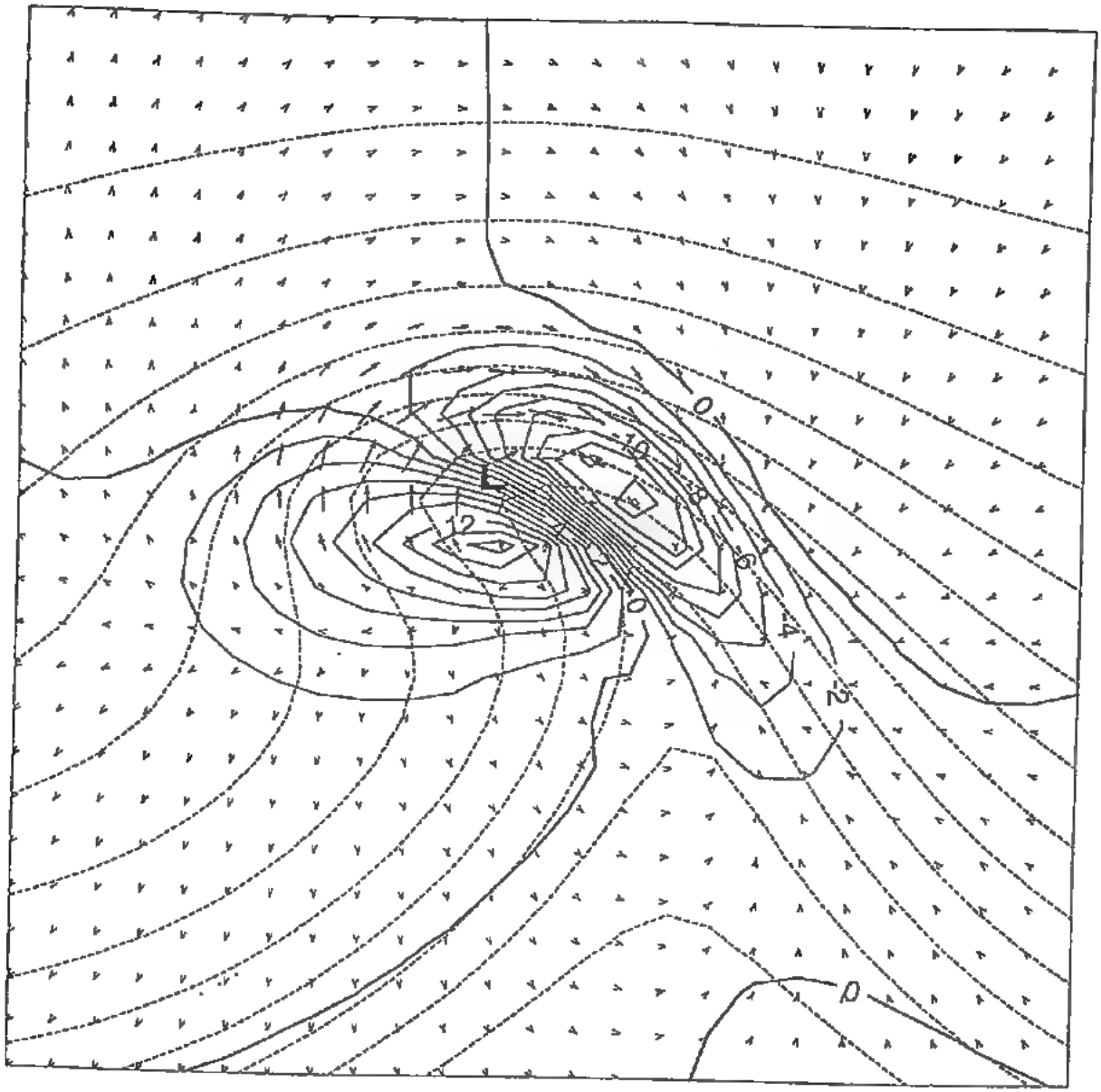

Fig. 3 QG forcing (continuous contours labelled in units of $10^{-16}\ m^{-1}\ s^{-3}$) and Q-vectors (maximum length equivalent to $2.0\times10^{-10}\ s^{-3}$) evaluated on the model grid within the inner domain shown in Fig.1. Potential temperature also shown by dashed contours (at intervals of 3 *K*).

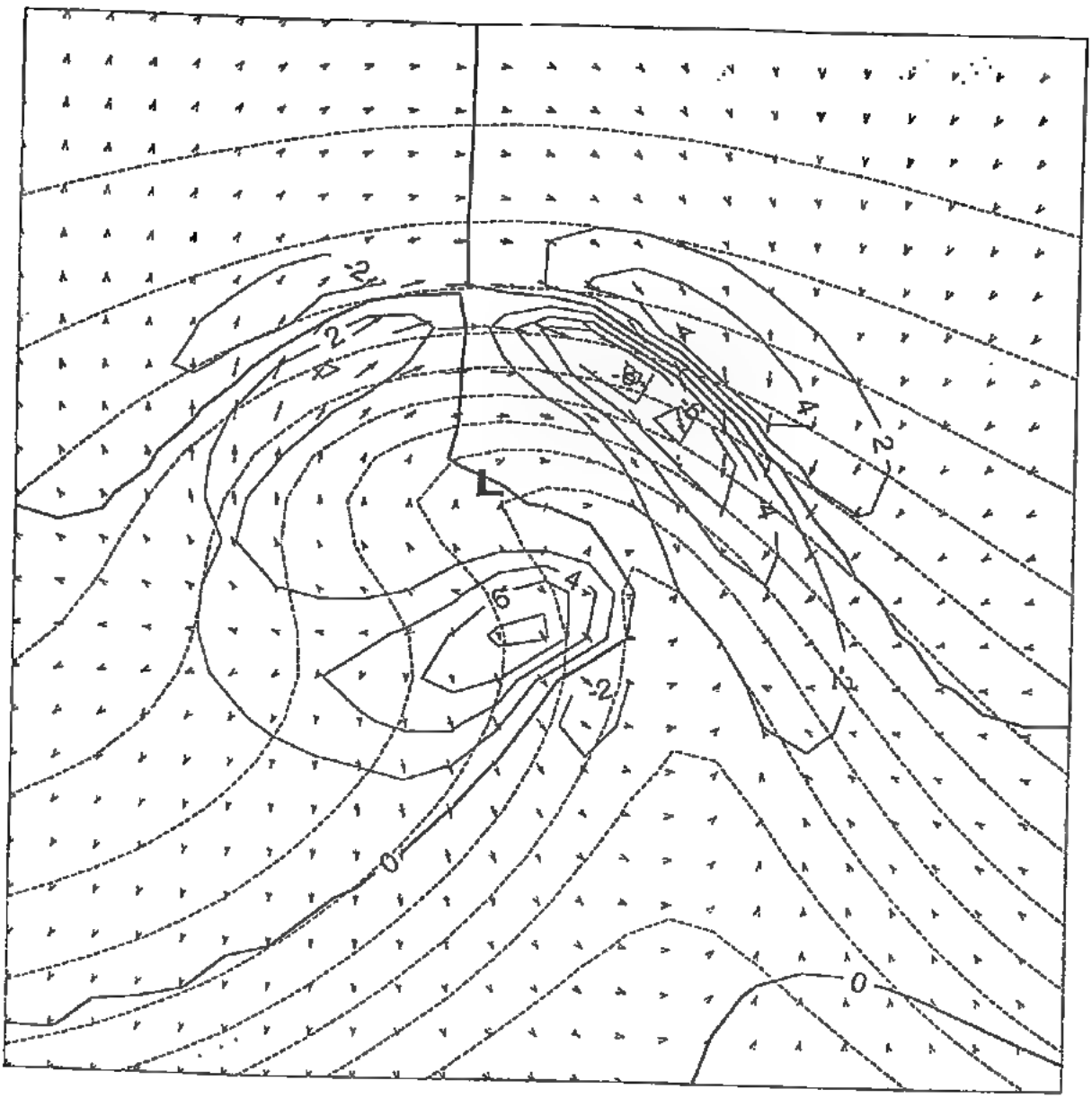

Fig. 4 SG forcing (continuous contours labelled in units of $10^{-16}\ m^{-1}\ s^{-3}$) and Q*-vectors (maximum length equivalent to $1.3\times10^{-10}\ s^{-3}$) evaluated on the model grid. Other details as in fig. 3.

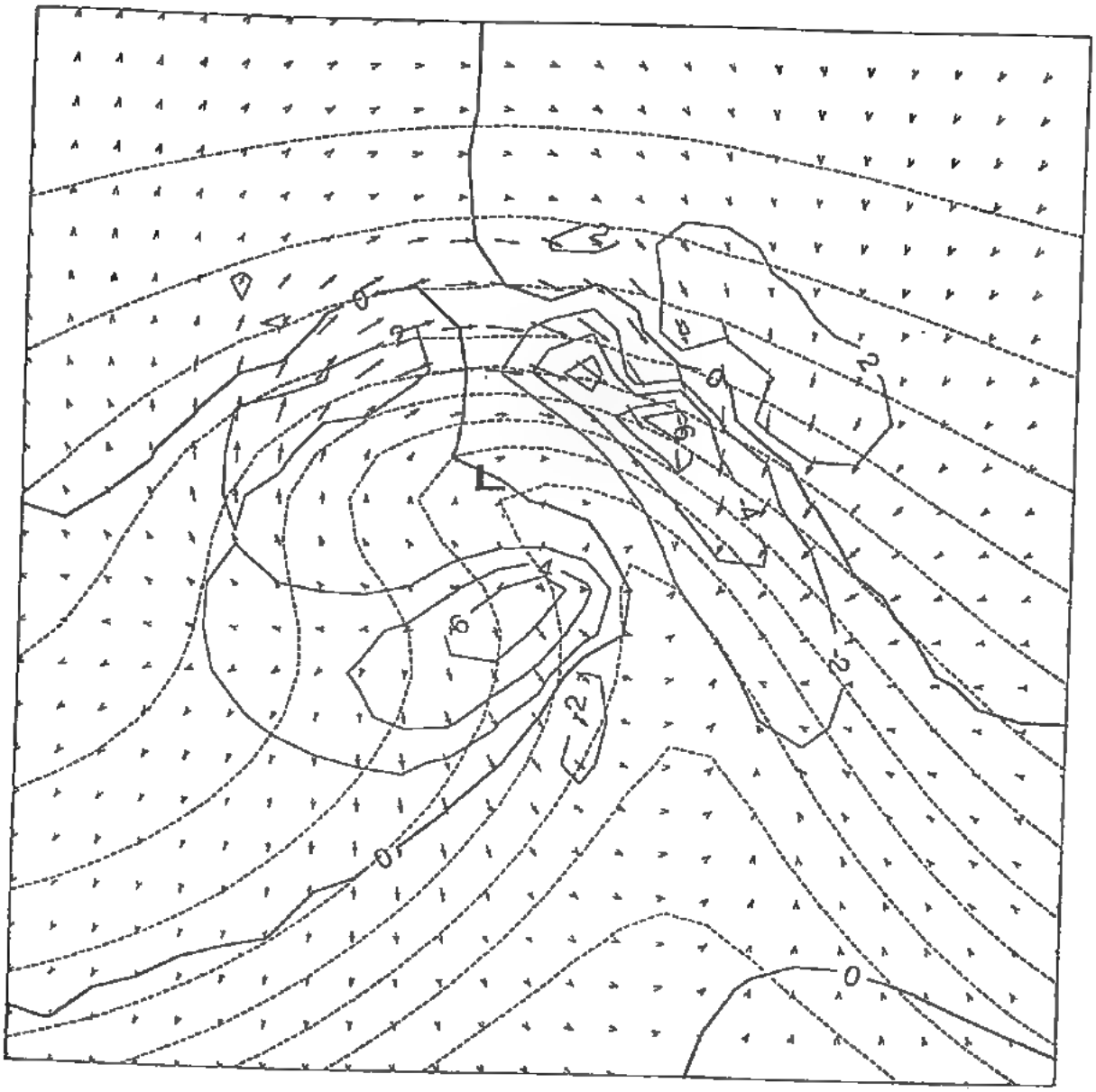

Fig. 5 Retrieval of Q*-vectors, SG forcing and potential temperature fields following forward and inverse GM transforms using a direct interpolation method. Plotting conventions as in Fig. 4.

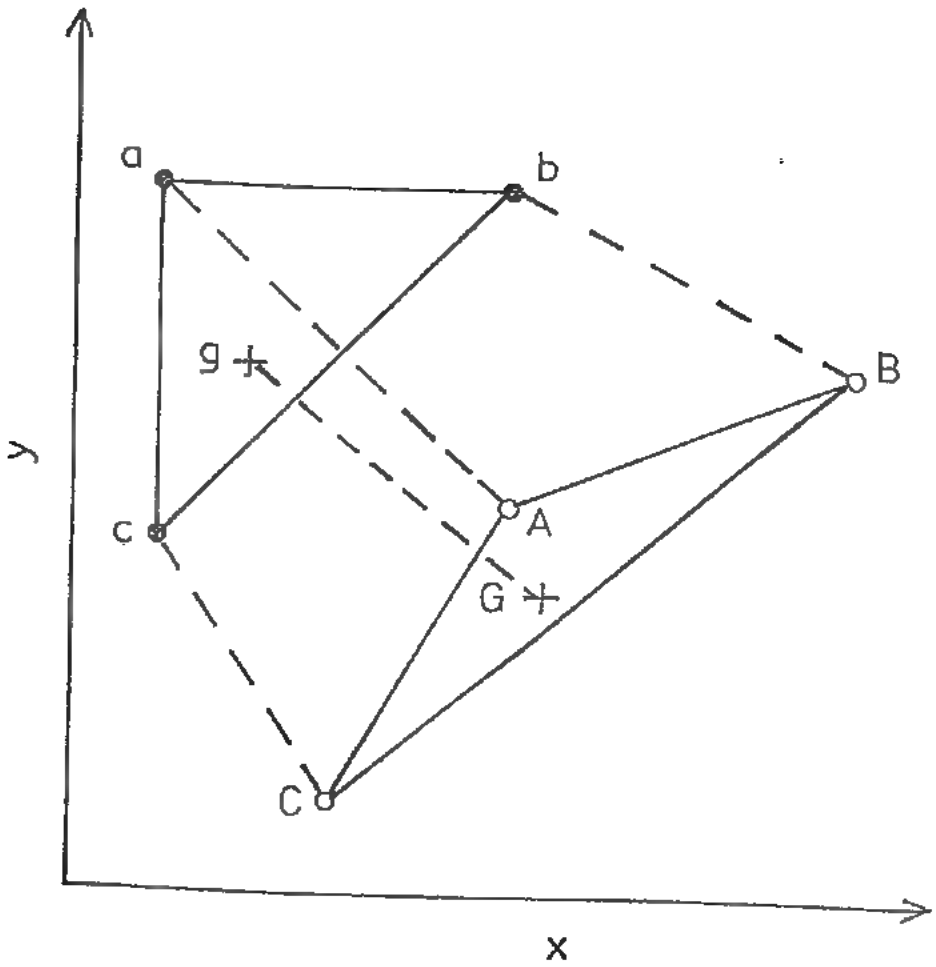

Fig. 6 A schematic representation of a GM coordinate transformation applied to a triangular local region (abc) in physical space, which generates a triangular local region (ABC) in GM space, subject to the assumption that the geostrophic velocity components vary linearly between the vertices of abc. This assumption also implies that any point G which is interior to ABC must map onto a point which is interior to abc under an inverse coordinate transform and that the geostrophic velocity components in GM space vary linearly between the vertices of ABC.

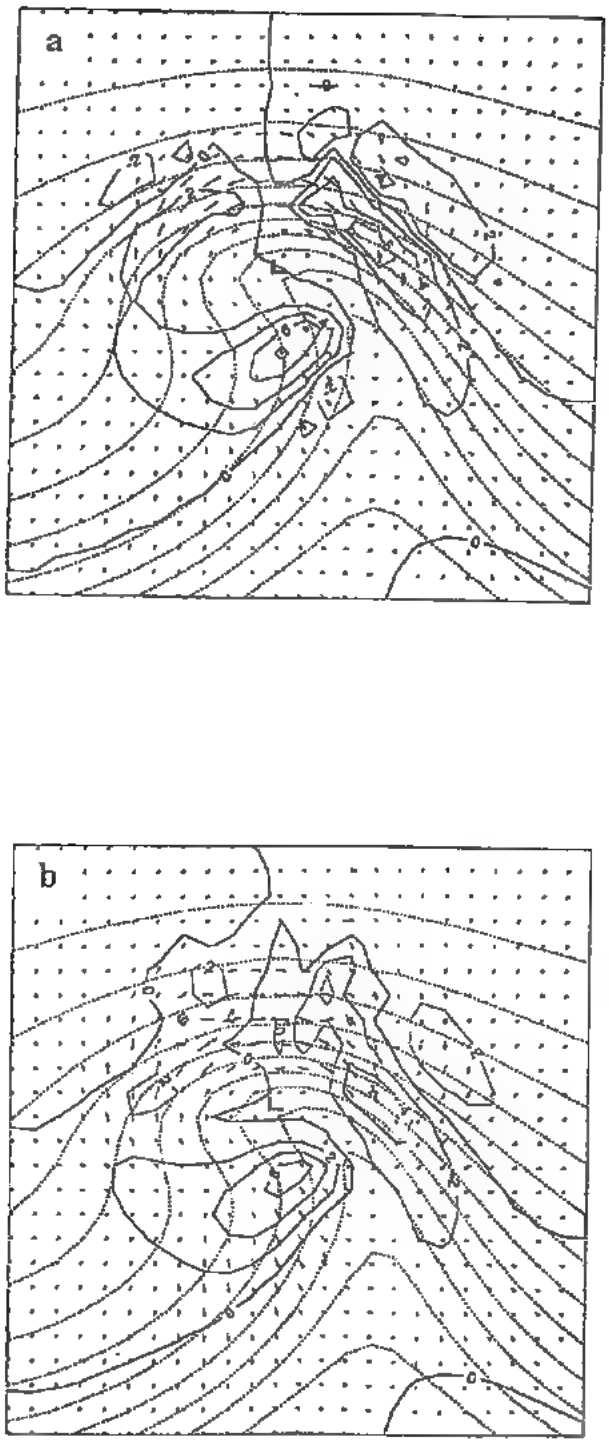

Fig. 7 Retrievals following forward and inverse GM transforms using an indirect interpolation method. a) Forward and inverse transforms applied to **Q***-vectors and SG forcing evaluated in model space; b) Forward transform applied to SG streamfunction ψ_g^* evaluated on the model grid, followed by inverse transform applied to **Q***-vectors and SG forcing evaluated on the GM grid from interpolated values of Ψ_g^*. Other details as in Fig. 4.

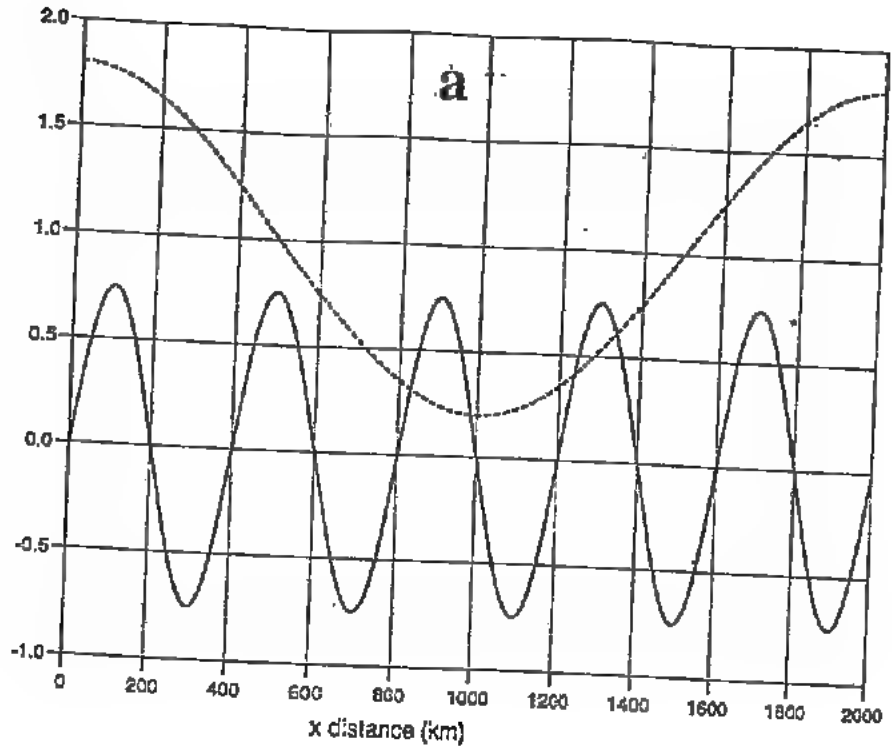

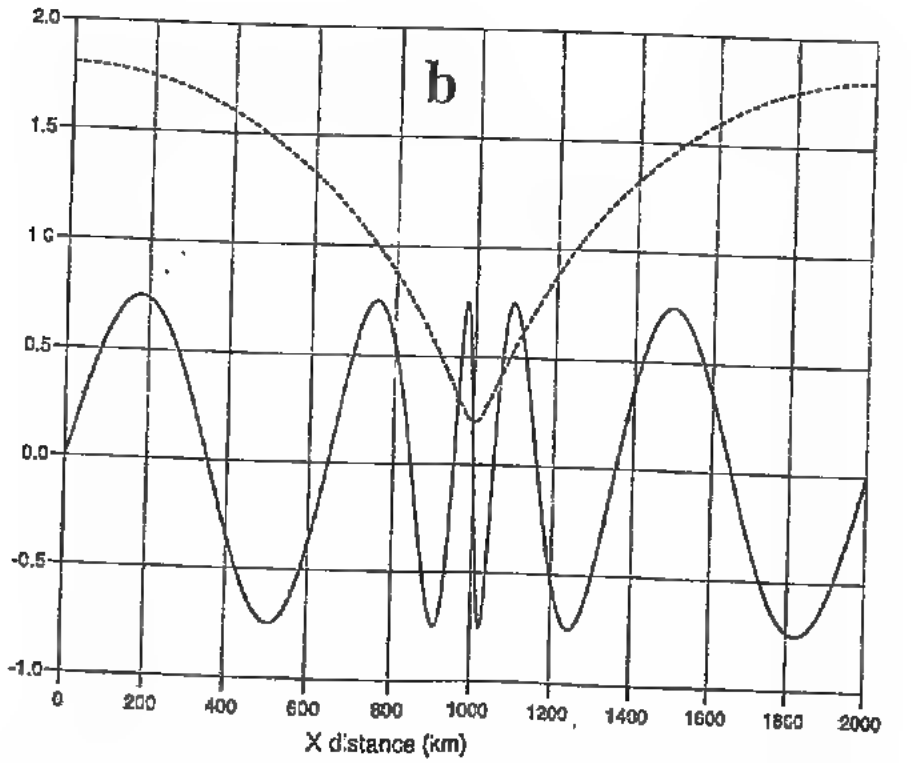

Fig. 8 One dimensional illustration of the scale-distortion effect of a GM coordinate transformation. In the upper panel (a), the continuous line represents a sinusoidal field sampled on the physical domain; the dashed line corresponds to the Jacobian of the horizontal transformation J $(=1+(1/f)\partial v_g/\partial x)$ associated with a sinusoidal variation in v_g along the x-direction. The lower panel (b) represents the structure of the field and the Jacobian of the GM coordinate transformation as seen in GM space.

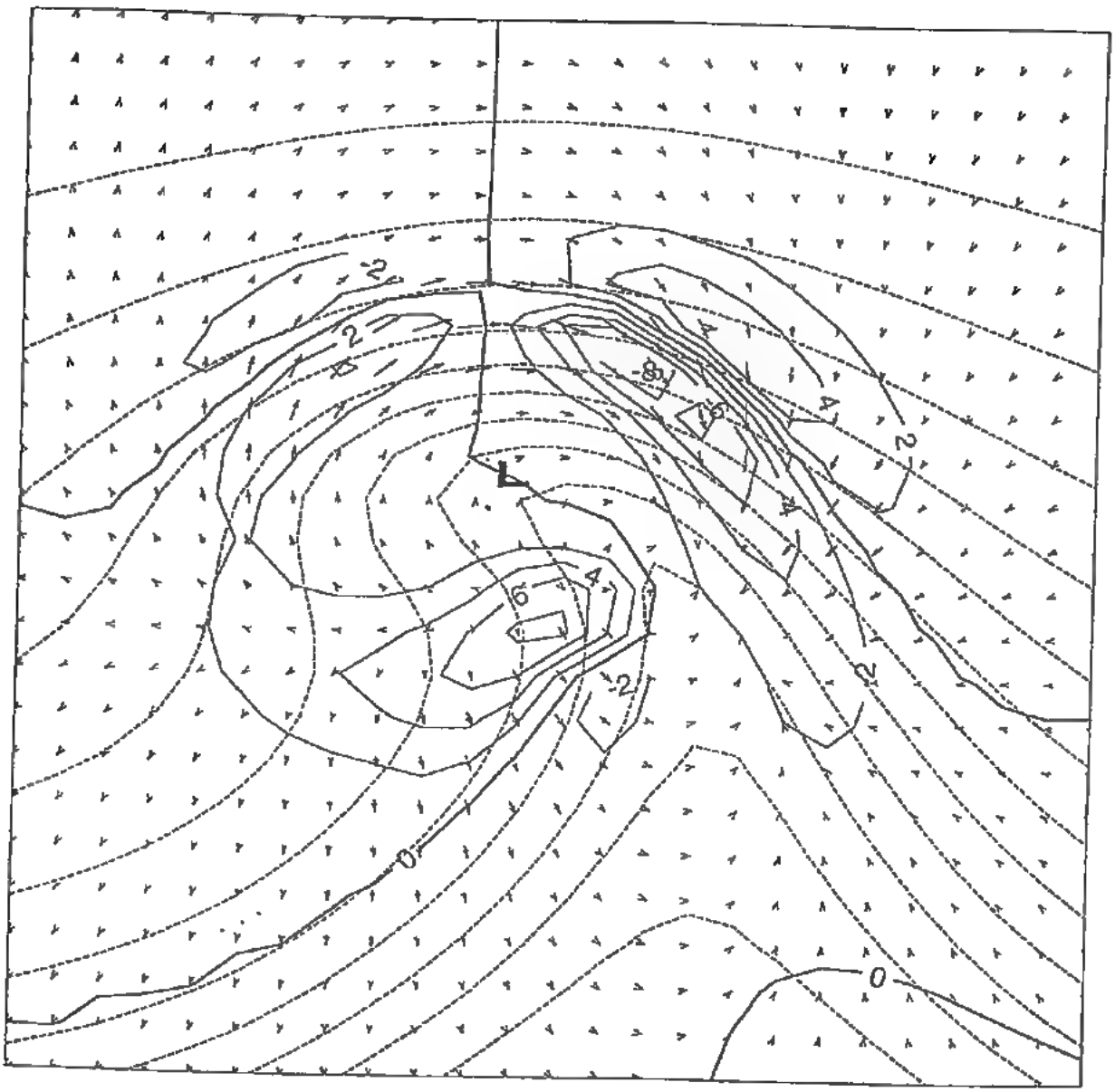

Fig. 9 Retrieval of Q*-vectors, SG forcing and potential temperature fields following forward and inverse GM transforms using indirect interpolation method when the grid spacing in GM space (25 km) is one quarter of that in model space (100 *km*). Plotting conventions as in Fig. 4.

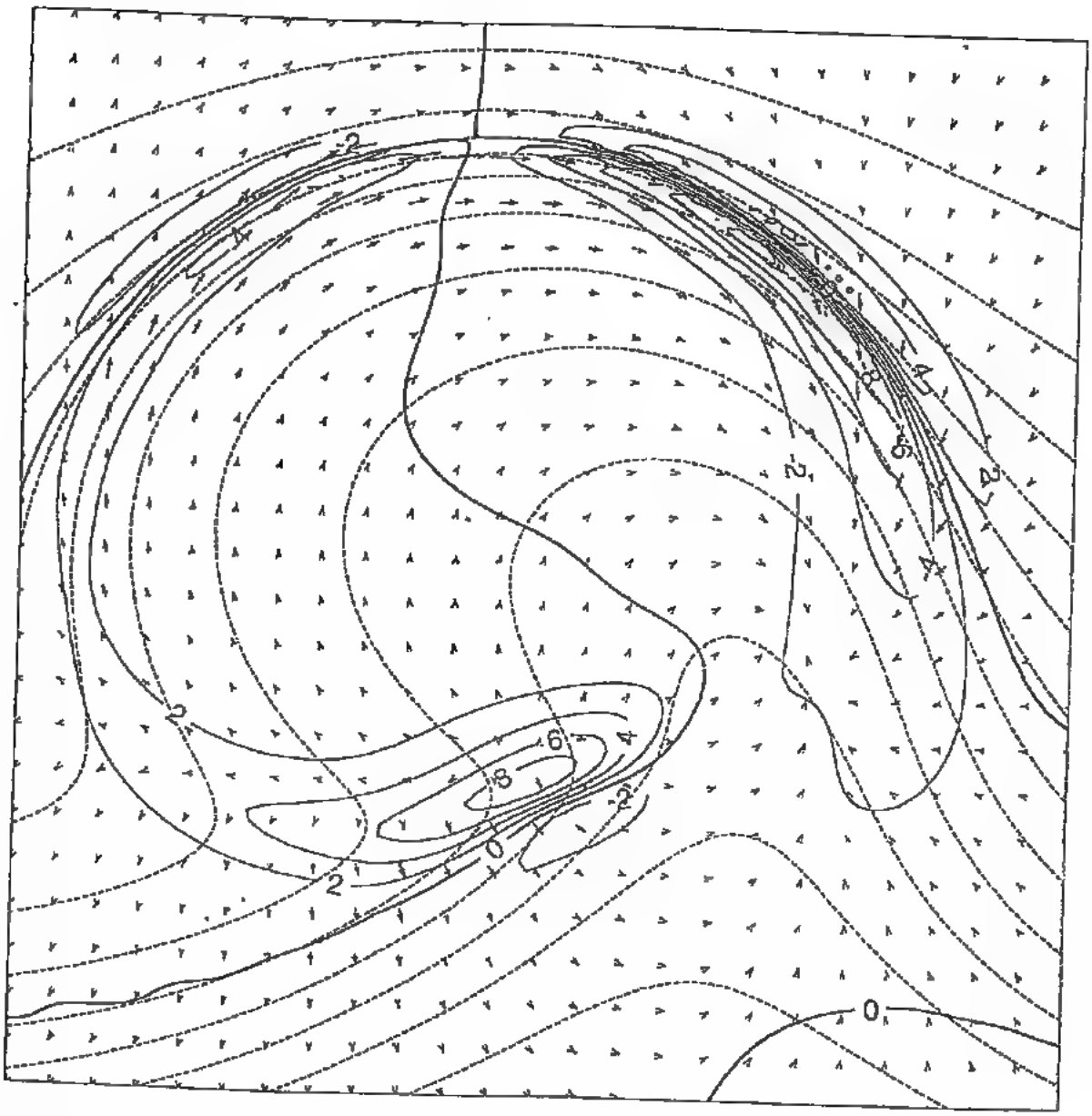

Fig. 10. SG forcing (continuous contours labelled in units of 10^{-16} m^{-1} s^{-3}) and potential temperature (dashed contours drawn at intervals of 3 K) on the GM coordinate domain (inner 2400 *km* by 2400 *km*), estimated using the indirect transform method with Δ_R=25 *km*. Also shown are **Q*** vectors plotted every 100 *km*.

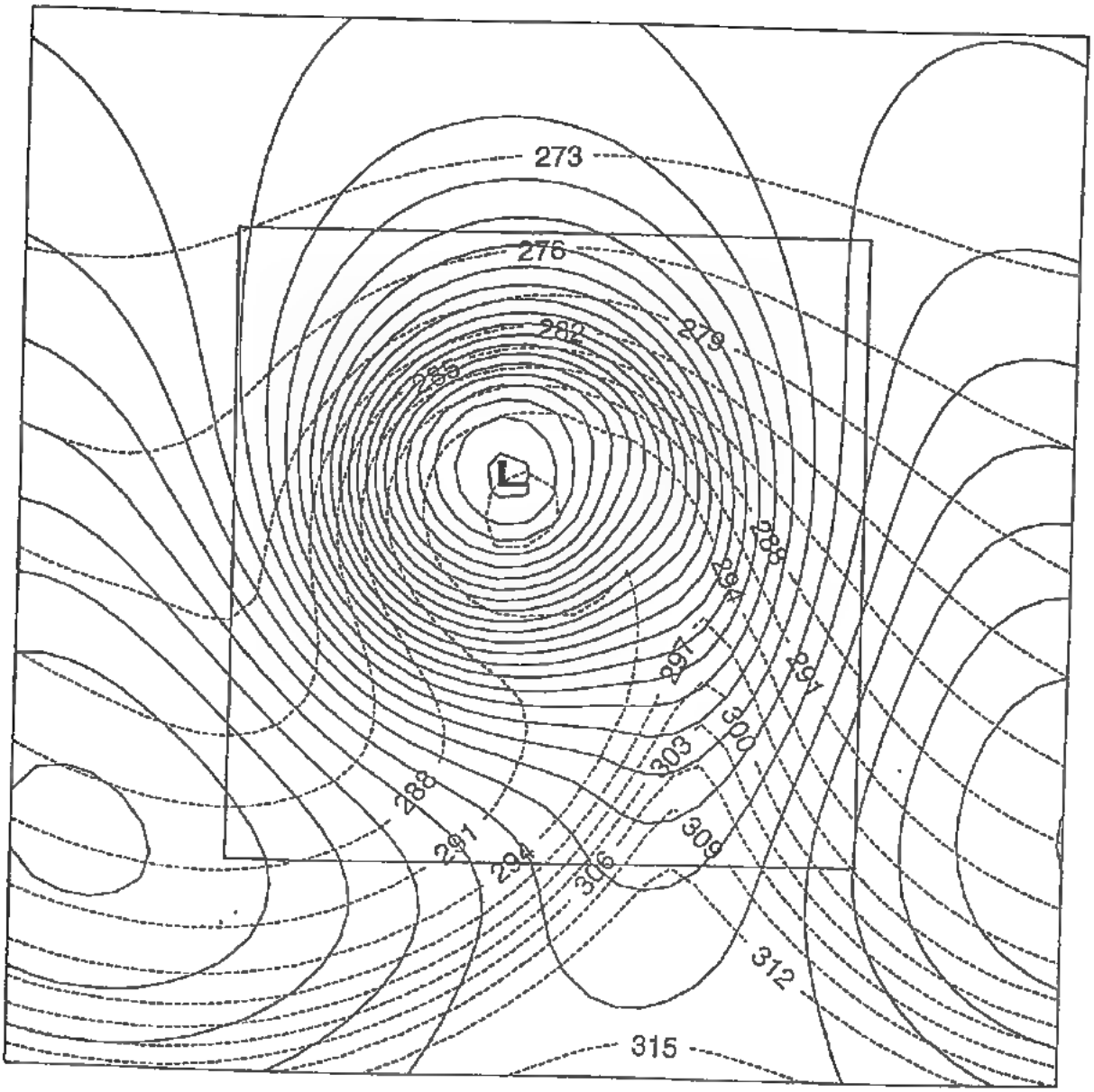

Fig. 11 Geostrophic streamfunction (continuous contours drawn every 3×10^6 $m^2\ s^{-1}$) and potential temperature (dashed contours labelled in units of degrees K) at day 8 of model integration. Other details as in Fig. 1.

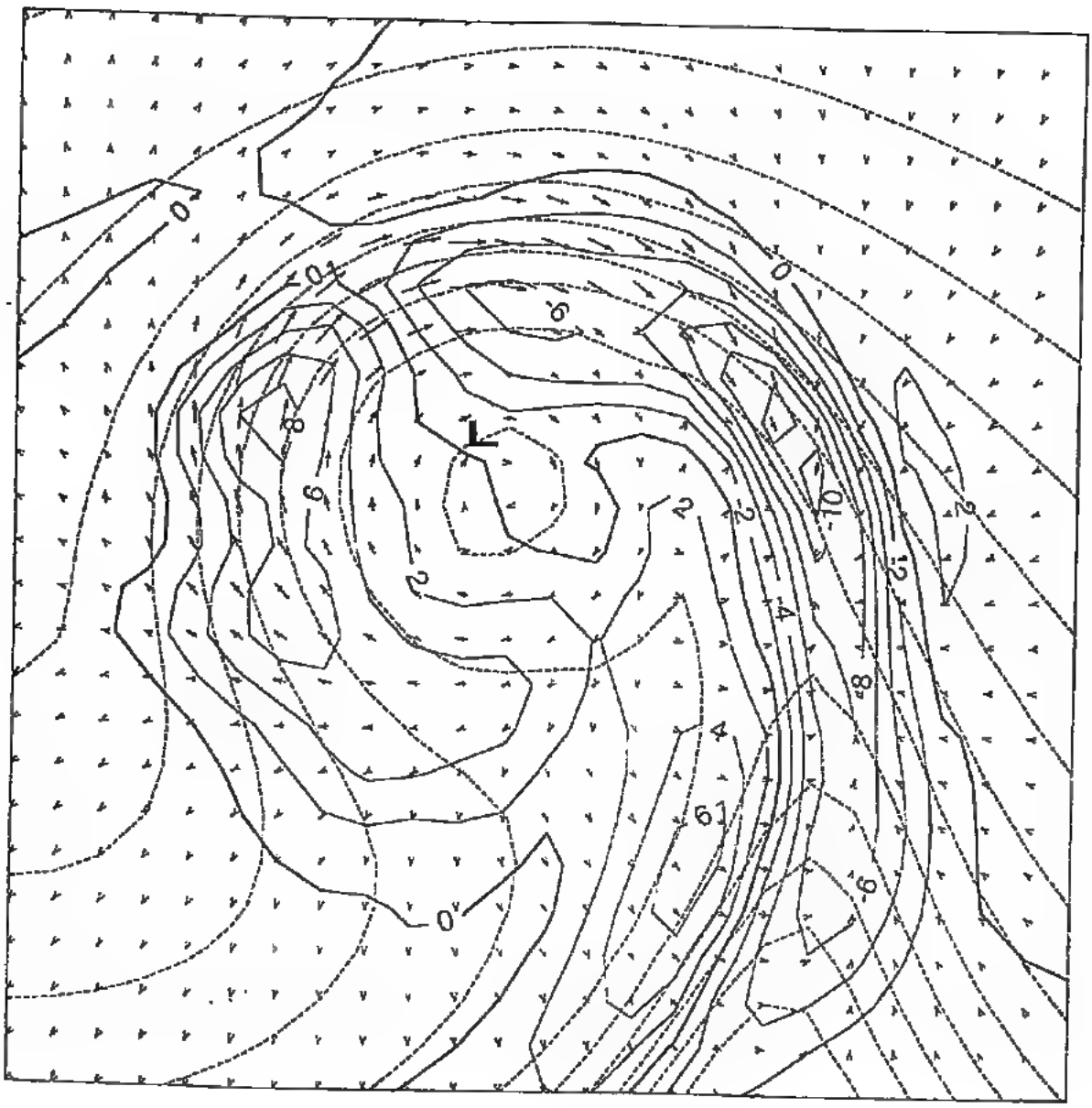

Fig. 12 QG forcing (continuous contours labelled in units of 10^{-16} m^{-1} s^{-3}) and Q-vectors (maximum length equivalent to 2.6×10^{-10} s^{-3}) evaluated on the model grid within the inner domain shown in Fig. 11. Potential temperature also shown by dashed contours (every 3 *K*).

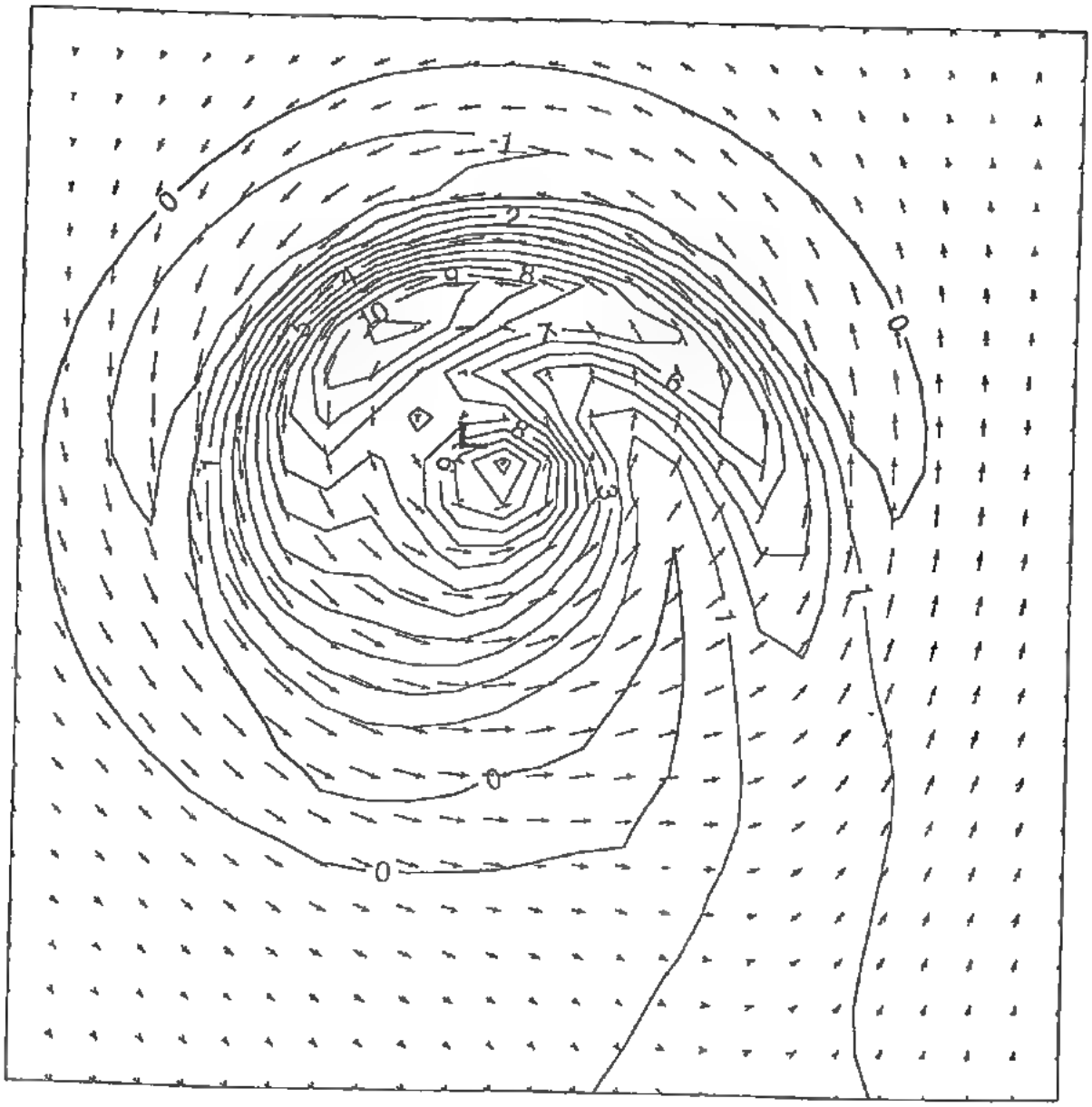

Fig. 13 Jacobian of the horizontal GM coordinate transformation within the inner region shown in Fig. 11. Contouring is in intervals of 1 with zero line marked bold. Also shown are geostrophic wind vectors (maximum length equivalent to 80 $m\ s^{-1}$) plotted at the model grid points.

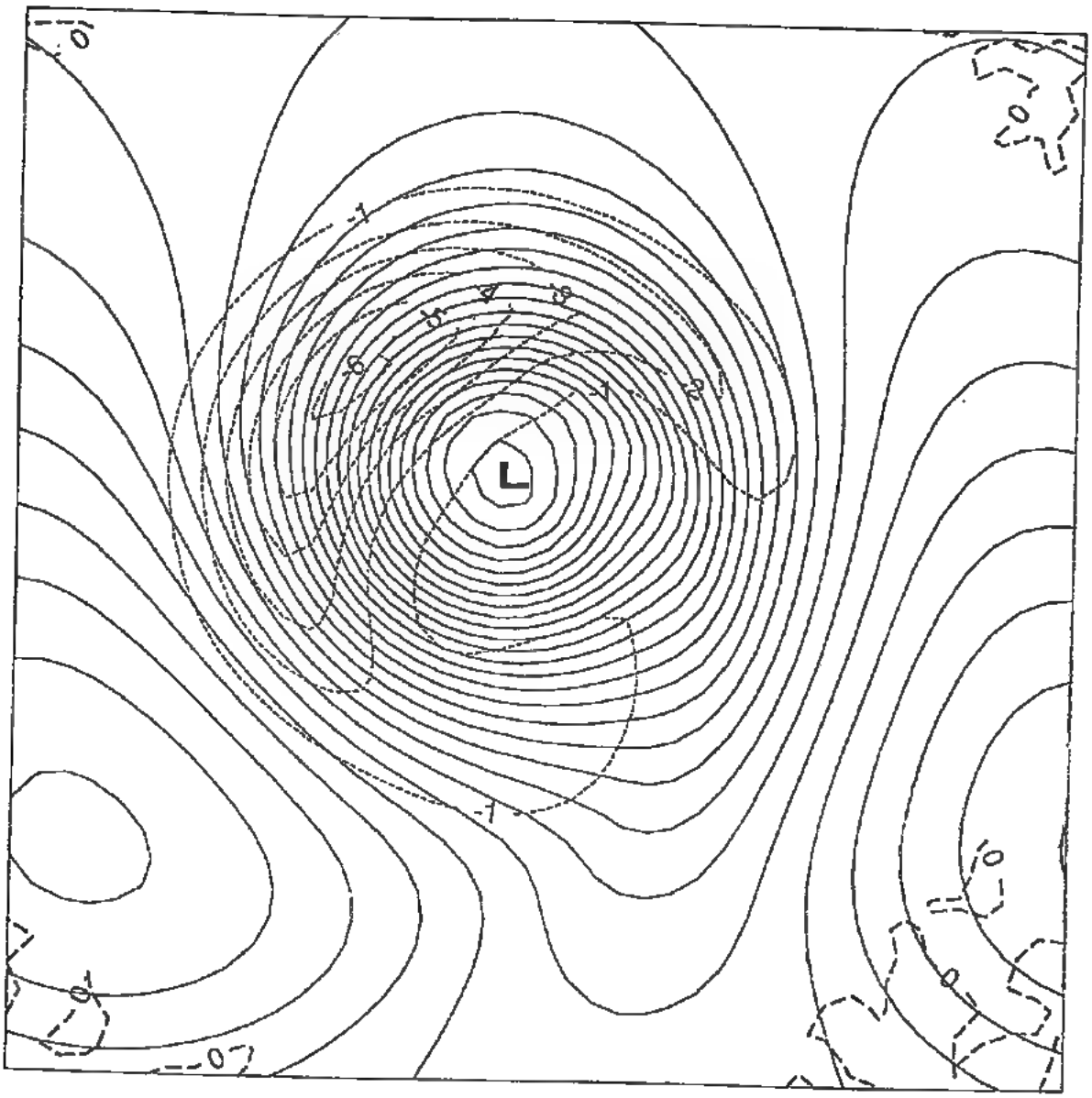

Fig. 14 Result of applying adjustment scheme to the day 8 model data so that J everywhere exceeds a minimum value of 0.3. Adjusted ψ_s field represented by continuous contours (every $3\times10^6\ m^2\ s^{-1}$); difference between adjusted and original field shown by dashed contours (labelled in units of $10^6\ m^2\ s^{-1}$. The domain of the figure is as in Fig. 1.

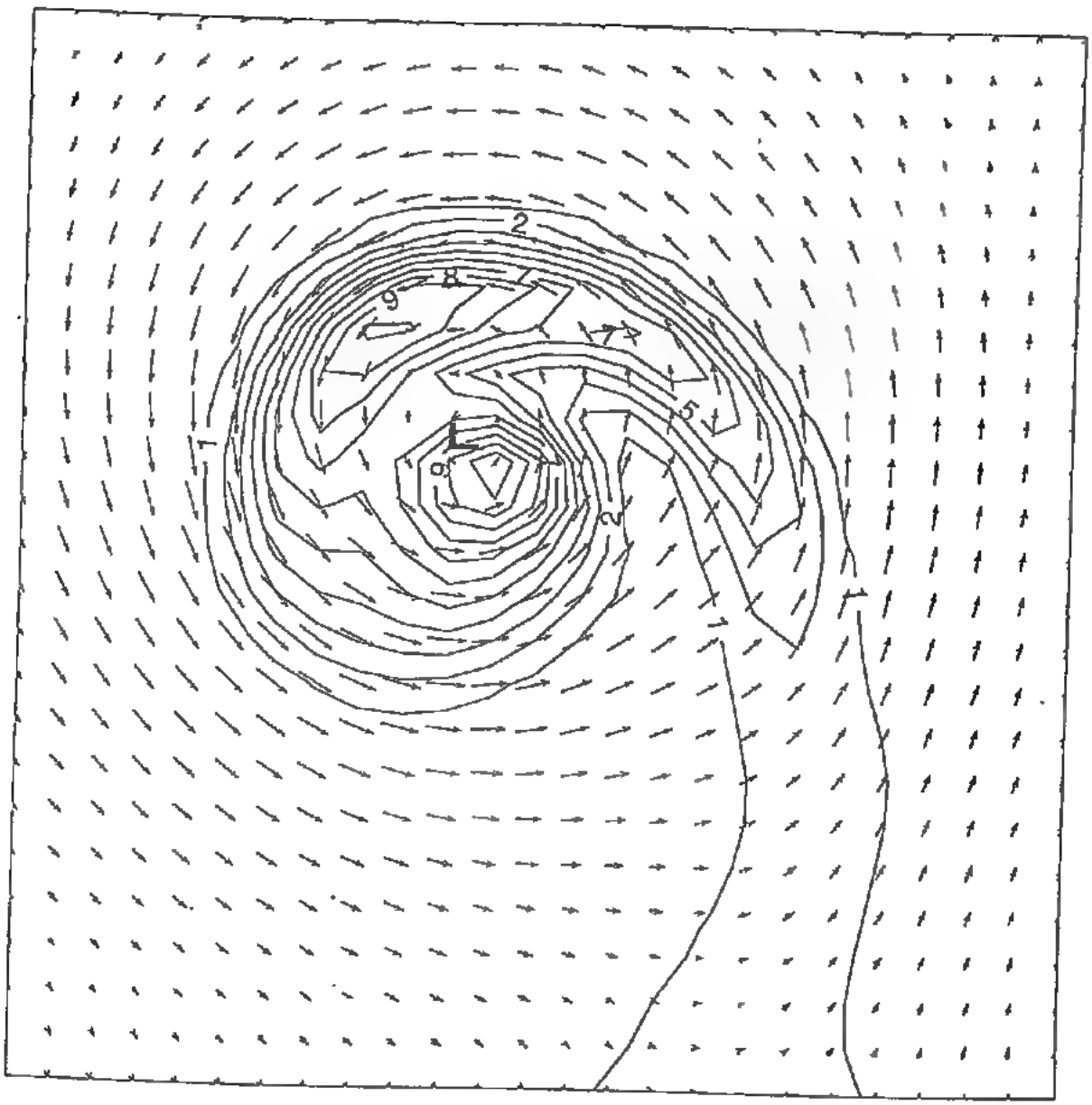

Fig. 15 Jacobian of the horizontal GM coordinate transformation within the inner region shown in Fig. 11, following adjustment. Other details as in Fig. 13.

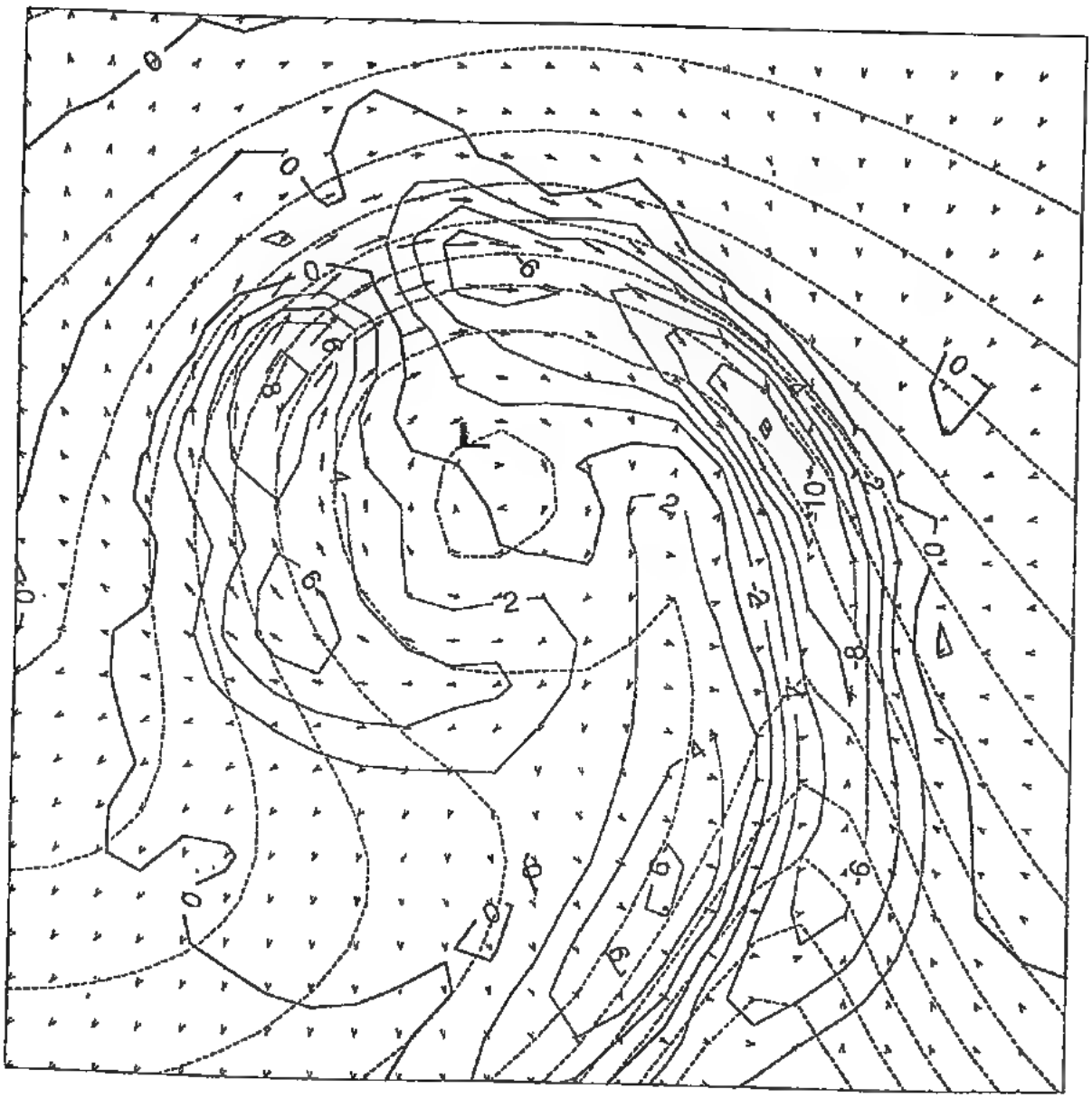

Fig. 16 QG forcing, Q-vectors and potential temperature evaluated on the model grid following adjustment. Other details as in Fig. 12.

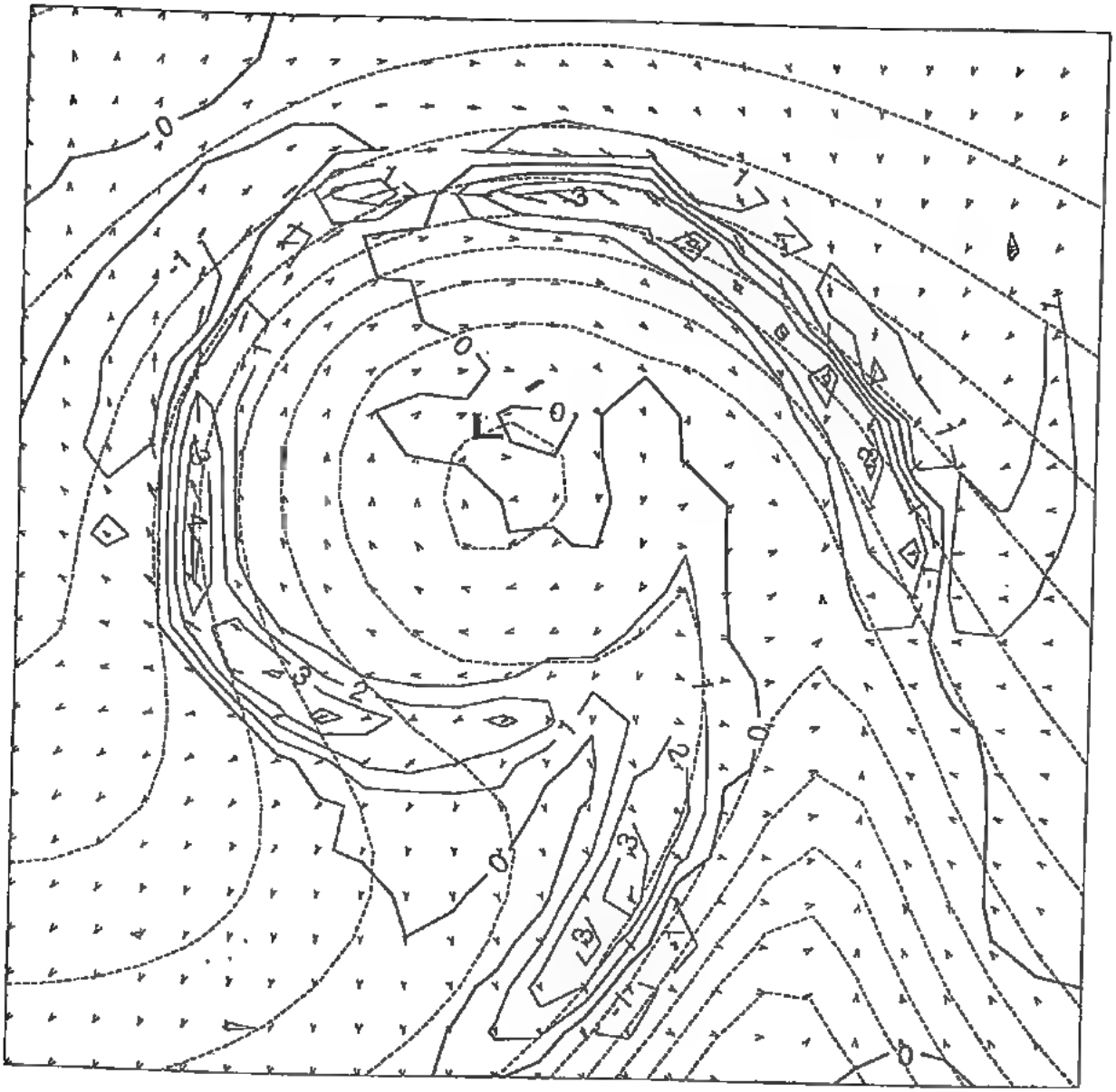

17

Fig. 17 SG forcing, Q*-vectors and potential temperature evaluated on the model grid following adjustment. Other details as in Fig. 12.

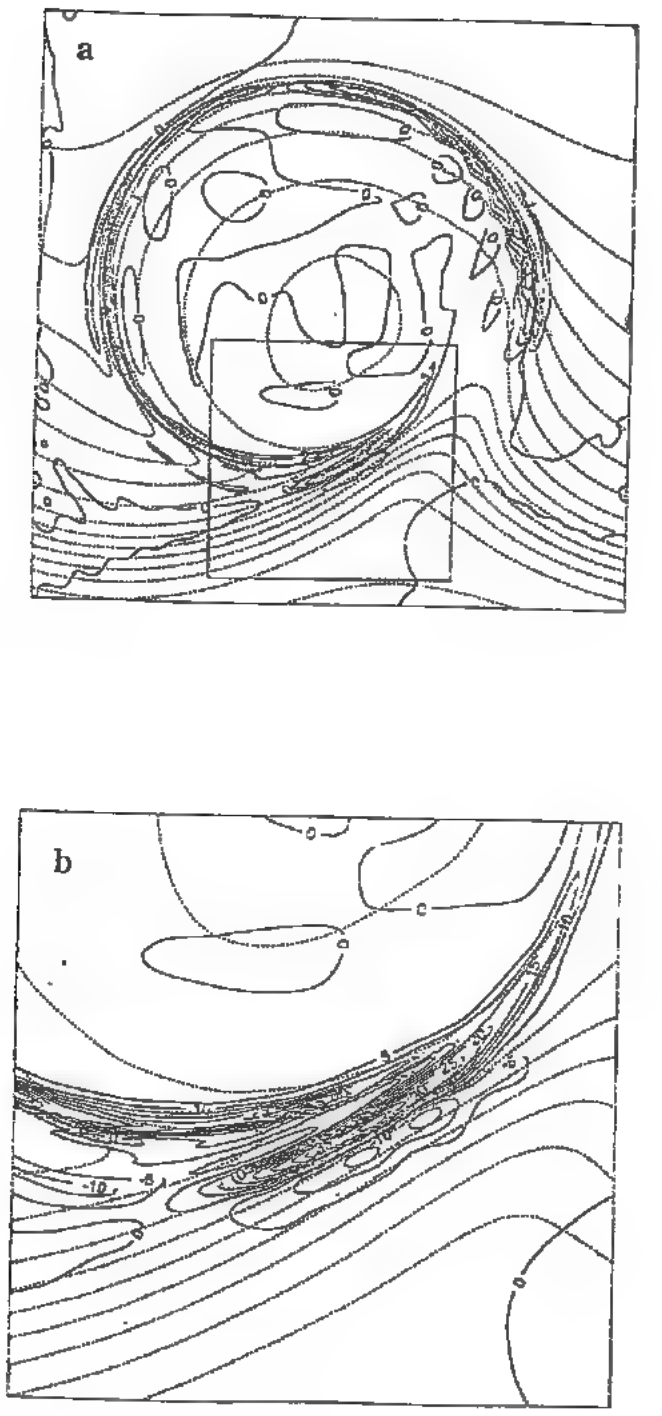

Fig. 18 SG forcing (continuous contours) and potential temperature (dashed contours) in GM space, based on forward interpolation of adjusted day 8 data by indirect method onto a 12.5 *km* resolution grid. a) 4000 *km* by 4000 *km* domain (F^* contoured every 1×10^{-15} m^{-1} s^{-3}); b) 1600 *km* by 1600 *km* inner domain, as identified in panel a) (F^* contoured every 5×10^{-16} m^{-1} s^{-3}). θ contours drawn every 3 *K* in both panels.

CURRENT JCMM INTERNAL REPORTS

This series of JCMM Internal Reports, initiated in 1993, contains unpublished reports and also versions of articles submitted for publication. The complete set of Internal Reports is available from the National Meteorological Library on loan, if required.

1. **Research strategy and programme**
   K A Browning et al
   January 1993

2. **The GEWEX Cloud System Study (GCSS)**
   GEWEX Cloud System Science Team
   January 1993

3. **Evolution of a mesoscale upper tropospheric vorticity maximum and comma cloud from a cloud-free two dimensional potential vorticity anomaly**
   K A Browning
   January 1993

4. **The global energy and water cycle**
   K A Browning
   July 1993

5. **Structure of a midlatitude cyclone before occlusion**
   K A Browning and N Roberts
   July 1993

6. **Developments in systems and tools for weather forecasting**
   K A Browning and G Szejwach
   July 1993

7. **Diagnostic study of a narrow cold frontal rainband and severe winds associated with a stratospheric intrusion**
   K A Browning and R Reynolds
   August 1993

8. **Survey of perceived priority issues in the parametrizations of cloud-related processes in GCMs**
   K A Browning
   September 1993

9. **The effect of rain on longwave radiation**
   I Dharssi
   September 1993

10. **Cloud microphysical processes - a description of the parametrization used in the large eddy model**
    H Swann
    October 1993

11. **An appreciation of the meteorological research of Ernst Kleinschmidt**
    A J Thorpe
    May 1992

12. **Potential vorticity of flow along the Alps**
    A J Thorpe, H Volkert and Dietrich Heimann
    August 1992

13. **The representation of fronts**
    A J Thorpe
    January 1993

14. **A parametrization scheme for symmetric instability: test for an idealised flow**
C S Chan and A J Thorpe
February 1993

15. **The Fronts 92 Experiment: a Quicklook Atlas**
Edited by T D Hewson
November 1993

16. **Frontal wave stability during moist deformation frontogenesis**
Part 1: Linear wave dynamics
C H Bishop and A J Thorpe
May 1993

17. **Frontal wave stability during moist deformation frontogenesis**
Part 2. The suppression of non-linear wave development
C H Bishop and A J Thorpe
May 1993

18. **Gravity waves in sheared ducts**
S Monserrat and A J Thorpe
October 1993

19. **Potential vorticity and the electrostatics analogy: quasi-geostrophic theory**
C Bishop and A J Thorpe
November 1993

20. **Recent advances in the measurement of precipitation by radar**
A J Illingworth
April 1993

21. **Micro-physique et givrage: cloud microphysics and aircraft icing**
A J Illingworth
May 1993

22. **Differential phase measurements of precipitation**
M Blackman and A J Illingworth
May 1993

23. **Estimation of effective radius of cloud particles from the radar reflectivity**
N I Fox and A J Illingworth
May 1993

24. **A simple method of Dopplerising a pulsed magnetron radar**
A Hua, A J Illingworth and J Eastment
November 1993

25. **Radiation and polar lows**
George C Craig
February 1994

26. **Collected preprints submitted to the International Symposium on the Life Cycles of Extratropical Cyclones; Bergen, Norway, 27 June - 1 July 1994**
April 1994

27. **Convective frontogenesis**
Douglas J Parker and Alan J Thorpe
April 1994

28. **Improved measurement of the ice water content in cirrus using a total water evaporator**
Philip R A Brown and Peter N Francis
April 1994

29. **Mesoscale effects of a dry intrusion within a vigorous cyclone**
K A Browning and B W Golding
April 1994

30. **GEWEX Cloud System Study, Science Plan**
May 1994

31. **Parametrization of momentum transport by convectively generated gravity waves**
R Kershaw
May 1994

32. **Mesoscale Modelling Newsletter No 5**
May 1994

33. **Observations of the mesoscale sub-structure in the cold air of a developing frontal cyclone**
K A Browning, S A Clough, C S A Davitt, N M Roberts and T D Hewson
May 1994

34. **Longwave radiative forcing of a simulated tropical squall line**
Imtiaz Dharssi
July 1994

35. **On the nature of the convective circulation at a kata-cold front**
K A Browning
September 1994

36. **Collective preprints of papers submitted to the COST-75 International Seminar on Advanced Weather Radar Systems, Brussels, 20-23 September 1994**
November 1994

37. **Use of satellite imagery to diagnose events leading to frontal thunderstorms: Parts I and II of a case study**
K A Browning and N M Roberts
November 1994

38. **The role of spaceborne millimetre-wave radar in the global monitoring of ice cloud**
P R A Brown, A J Illingworth, A J Heymsfield, G M McFarquhar, K A Browning and M Gosset
December 1994

39. **Potential vorticity inversion**
Michal Ziemianski
October 1994

40. **Theory of mature tropical cyclones; a comparison between Kleinschmidt (1951) and Emanuel (1986)**
Suzanne L Gray
December 1994

41. **Dispersion and removal of pollutants during the passage of an atmospheric frontal system**
N R Gimson
December 1994

42. **The role of snow sublimation in frontogenesis**
D J Parker and A J Thorpe
December 1994

43. **Potential vorticity and the electrostatics Analogy: Ertel-Rossby formulation**
A J Thorpe and C H Bishop
December 1994

44. **Mesoscale aspect of extratropical cyclones: an observational perspective**
K A Browning
January 1995

45. **A polar low outbreak: evolution and mesoscale structures**
T D Hewson, G C Craig and C Claud
February 1995

46. **Generation of near-surface gusts of deep convection**
K Nakamura and R Kershaw
April 1995

47. **Attribution concepts applied to the Omega Equation**
S A Clough, C S A Davitt and A J Thorpe
June 1995

48. **Parametrization of mixed-phase cloud and precipitation**
Susan P Ballard and M Gerard Hutchinson
June 1995

49. **Short-range forecasting of stratocumulus: initialization prediction**
Susan P Ballard, Simon D Jackson and B Macpherson
June 1995

50. **Contributions of the JCMM/Dept of Meteorology Radar Group to the 27th AMS Radar Meteorology Conference, Vail October 1995**
June 1995

51. **Cold pools in shear**
Douglas J Parker
September 1995

52. **High-resolution analysis of frontal fracture**
K A Browning, S P Ballard and C S A Davitt
September 1995

53. **The albedo of broken cloud fields: calculations using a modified two stream radiation code**
Imtiaz Dharssi and Roy Kershaw
October 1995

54. **Parametrization of momentum transport by convection. I: theory and cloud modelling results**
R Kershaw and D Gregory
November 1995

55. **Variation of frontal structure along a cold front**
K A Browning and N M Roberts
November 1995

56. **Secondary frontal waves**
Douglas Parker
December 1995

57. **Objective fronts**
T D Hewson
March 1996

58. **Mesoscale analysis of the activation of a cold front during cyclogenesis**
K A Browning, N M Roberts and A J Illingworth
June 1996

59. **Investigation of different representations of rain in a 1-d evaporation model**
H Swann
May 1996

60. **Parametrization of diabatic processes in the inversion of the omega-equation**
M Athanassiadou and A J Thorpe
June 1996

61. **The role of the environmental flow in the development of secondary frontal cyclones**
I A Renfrew, A J Thorpe and A Joly
June 1996

62. **Consequences of the geostrophic momentum approximation on barotropic instability**
S Malardel, A J Thorpe and A Joly
June 1996

63. **Contributions to the AMS/RMS Conference on Mesoscale Processes**
Reading, 9-13 September 1996

64. **Vorticity and potential vorticity in stratified flows interacting with an isolated obstacle**
Jorge A Gutiérrez and A J Thorpe
September 1996

65. **Triple point development: two case studies**
Douglas Parker
September 1996

66. **Radar observations of wind-shear splitting within evolving atmospheric Kelvin-Helmholtz billows**
D Chapman and K A Browning
April 1997

67. **Cold frontal structure derived from radar wind profilers**
K A Browning, D Jerrett, J Nash, T Oakley and N M Roberts
May 1997

68. **The dry intrusion and its effect on the frontal, cloud and precipitation structure of extratropical cyclones**
K A Browning - Text of invited special lecture at the Spring Conference
of the Meteorological Society of Japan, University of Tsukuba, 22 May 1997

69. **Met. Office Unified Model data, diagnostics, graphics programs, and other observational data available from the JCMM through the aegis of the Universities Weather Research Network (UWERN).** (Plus supplement)
Peter Panagi and Ed Dicks
June 1997

70. **Contributions of the JCMM/Dept of Meteorology Radar Group to the 28th AMS Radar Meteorology Conference.** Austin, Texas
September 1997

71. **Sensitivity of short-range weather forecasts to local potential vorticity modifications**
Meral Demirtas and Alan Thorpe
July 1997

72. **Objective identification of frontal wave cyclones**
T D Hewson
August 1997

73. **Attribution and its application to mesoscale structure associated with tropopause folds**
A J Thorpe
September 1997

74. **The role of the environmental flow in the development of secondary frontal cyclones**
Ian A Renfrew, Alan J Thorpe and Craig H Bishop
September 1997

75. **Potential vorticity: a short history of its definitions and uses**
Alan J Thorpe and Hans Volkert
September 1997

76. **Superposing semi-geostrophic potential vorticity anomalies**
H R Birkett and A J Thorpe
September 1997

77. **Short period forecasting of catchment-scale precipitation.**
Part 1: the role of Numerical Weather Prediction
M A Pedder, M Haile and A J Thorpe
September 1997

78. **Verification of the tracking technique used in an experimental cloud motion wind inferring system**
Z Wang, K A Browning and G A Kelly
October 1997

79. **A preliminary study of Fourier series analysis for cloud tracking with GOES high temporal resolution images**
Z Wang
October 1997

80. **Analysis of an ex-tropical cyclone after reintensifying as a warm-core extratropical cyclone**
K A Browning, G Vaughan and P Panagi
November 1997

81. **A JCMM overview of FASTEX IOPs**
S A Clough, H W Lean, N M Roberts, H Birkett, J-P Chaboureau, R Dixon, M Griffiths, T D Hewson and A Montani
January 1998

82. **Programs for PV inversion and modification**
Meral Demirtas
December 1997

83. **Release of potential shearing instability in warm frontal zones**
D Chapman and K A Browning
February 1998

84. **The European Cloud-Resolving Modelling Programme (EUCREM)**
Summary Report from the coordinator
P W White
April 1998

85. **A frontal wave database**
T D Hewson
April 1998

86. **Layering observed in dropsoundings from IOP 1 of Fronts 92**
S A Clough
May 1998

87. **Use of wind-shear displays for Doppler radar data**
D Chapman and K A Browning
May 1998

88. **Radar estimates of rainfall rates at the ground in bright band and non-bright band events**
T J Smyth and A J Illingworth
June 1998

89. **Correction for attenuation of radar reflectivity using polarisation data**
T J Smyth and A J Illingworth
June 1998

90. **The effects of convection on chemical reactions and precipitation scavenging**
Neil R Gimson
July 1998

91. **How to use the display program DISP**
Nigel Roberts
August 1998

92. **Conceptual models of cyclogenesis**
Adrian T Semple
August 1998

93. **Observations of oblate hail using dual polarisation radar and implications for hail detection schemes**
T J Smyth, T M Blackman and A J Illingworth
September 1998

94. **The semigeostrophic diagnosis of vertical motion. Part I: Formulation and co-ordinate transformations**
Mike A Pedder and Alan J Thorpe
September 1998

Met Office Joint Centre for Mesoscale Meteorology Department of Meteorology
University of Reading PO Box 243 Reading RG6 6BB United Kingdom
Tel: +44 (0)118 931 8425 Fax: +44 (0)118 931 8791
www.metoffice.com